INTRASEASONAL VARIABILITY IN THE FAR-EAST PACIFIC: INVESTIGATION OF THE ROLE OF AIR-SEA COUPLING IN A REGIONAL COUPLED MODEL

R. Justin Small[1,2], Shang-Ping Xie[2,3], Eric D. Maloney[4] , Simon P. deSzoeke[5] and Toru Miyama[6]

[1] *Jacobs Technology, Naval Research Laboratory,*
Code 7320, Building 1009, Stennis Space Center, MS 39529, USA

[2] *International Pacific Research Center, POST 401, 1680 East-West Rd,*
University of Hawaii, Honolulu, HI 96822, USA.

[3] *Department of Meteorology, HIG350, School of Ocean and Earth Science and Technology,*
2525 Correa Rd, University of Hawaii, Honolulu, HI 96822, USA.

4 Department of Atmospheric Sciences, Colorado State University, Fort Collins

[5] *College of Oceanic and Atmospheric Sciences, Oregon State University, 104 COAS Admin. Bldg.,*
Corvallis, OR 97331-5503, USA.

[6] *Frontier Research for Global Change, Yokohama, Japan*

Corresponding author address: Dr R Justin Small, Naval Research Laboratory,
Code 7320, Building 1009, Stennis Space Center, MS 39529, USA.
e-mail: small.ctr.uk@nrlssc.navy.mil
Telephone: 1-228-688-4974 fax 1-228-688-4759

Abstract

Intraseasonal variability in the eastern Pacific warm pool in summer is studied, using a regional ocean-atmosphere model, a linear baroclinic model, and satellite observations. The atmospheric component of the model is forced by lateral boundary conditions from reanalysis data. The aim is to quantify the importance to atmospheric deep convection of local air-sea coupling. In particular, the effect of sea surface temperature (SST) anomalies on surface heat fluxes is examined.

Intraseasonal (20-90 day) east Pacific warm-pool zonal wind and OLR variability in the regional coupled model are correlated at 0.8 and 0.6 with observations, respectively, significant at the 99% confidence level. The strength of the intraseasonal variability in the coupled model, as measured by the variance of outgoing longwave radiation, is close in magnitude to that observed, but with a maximum located about 10º further west. East Pacific warm pool intraseasonal convection and winds agrees in phase with those from observations, suggesting that remote forcing at the boundaries associated with the Madden-Julian Oscillation (MJO) determines the phase of intraseasonal convection in the east Pacific warm pool.

When the ocean model component is replaced by weekly reanalysis SST in an atmosphere-only experiment, there is a slight improvement in the location of the highest OLR variance. Further sensitivity experiments with the regional atmosphere-only model in which intraseasonal SST variability is removed indicate that convective variability has only a weak dependence on the SST variability, but a stronger dependence on the climatological mean SST distribution. A scaling analysis confirms that wind speed anomalies give a much larger contribution to the intraseasonal evaporation signal than SST anomalies, in both model and observations.

A linear baroclinic model is used to show that local feedbacks would serve to amplify intraseasonal convection and the large-scale circulation. Further, Hovmöller diagrams reveal that whereas a significant dynamic intraseasonal signal enters the model domain from the west, the strong deep convection mostly arises within the domain. Taken together, the regional and linear model results suggest that in this region remote forcing and local convection-circulation feedbacks are both important to the intraseasonal variability, but ocean-atmosphere coupling has only a small effect. Possible mechanisms of remote forcing are discussed.

1. Introduction

Intraseasonal variability in the tropics is dominated by the Madden Julian Oscillation (MJO: Madden and Julian 1994; Zhang 2005). The MJO not only impacts tropical precipitation and extreme events (e.g. Barlow and Salstein 2006; Maloney and Shaman 2008; Bessafi and Wheeler 2006), but also affects midlatitude weather (e.g. Higgins et al. 1999; Bond and Vecchi 2003). It is well known that many global Atmospheric General Circulation Models (AGCM) and Coupled General Circulation Models (CGCM) have difficulty simulating the MJO. When compared to observations, the models typically exhibit weak intraseasonal precipitation variance, little coherence between winds and precipitation anomalies, and a spectrum that is too broad, with the ratio of eastward to westward power being too small (Slingo et al. 1996; Lin et al 2006; Zhang et al. 2006). Problems with the MJO simulation are often attributed to inadequacies of the cumulus parameterization (Slingo et al. 1996; Lin et al. 2006).

The role of SST, and more generally, air-sea interaction, in the MJO cycle has been studied by a number of authors using coupled model experiments, with varying results, as reviewed by Hendon (2005). Coupling was only found to improve the simulations when the atmospheric model had a good representation of the phase relationship between insolation and evaporation (discussed by Hendon 2000). Such improvements were found by Maloney and Kiehl (2002a), who coupled an AGCM to a slab ocean model, and studied the impact on east Pacific intraseasonal precipitation, and Inness and Slingo (2003a) who used a coupled general circulation model and found improved simulations of Indian Ocean variability compared to results from an atmosphere-only model forced by slowly varying

SST fields. In contrast the study of Grabowski (2006) showed a weak dependence of the MJO on SST, in a coupled aquaplanet/slab-ocean model which employed superparameterization of cumulus convection. He suggested that the dominant process in his model was a feedback between convection and free-tropospheric moisture amount, with SST-convection feedbacks playing a much smaller role.

From satellite and buoy observations, Maloney et al. (2008) found that MJO-related SST variations of 0.8-1.0^{o}C occur in the Eastern Pacific warm pool, driven by latent heat and short wave flux variations. In the east Pacific, warm SST lead precipitation by about 10 days, whilst the SST cooled during MJO convective events. Maloney and Kiehl (2002b) suggested that SST-induced moisture convergence and oceanic heat content anomalies helped precondition the atmosphere for convection.

Idealized column models show that under certain conditions, an unforced oscillation of precipitation and SST can be obtained with an intraseasonal period in a cycle that resembles a recharge-discharge oscillation (e.g. Sobel and Gildor 2003). The behavior is highly dependent on the cloud-radiative feedback parameter (which can also be thought to represent wind-induced surface flux feedbacks), and convective timescale, and instability on intraseasonal timescales was found to be greatest for mixed layer depths in the range of 10-20 m,. If mixed layer depth goes to zero in a version of the model with prescribed intraseasonal wind speed forcing, effectively shutting off the wind-evaporation feedback, model intraseasonal variability decreases dramatically (e.g. Maloney and Sobel 2004).

Recently, coupled regional models have emerged as an alternative tool to investigate the effect of large scale variability on specific regions (Xie et al. 2007; Seo et al. 2007). A regional model has the advantage that propagating signals associated with the large-scale, hemispheric MJO can pass into the domain through the lateral boundary conditions in the atmosphere, and also possibly via oceanic pathways (Kessler et al. 1995). Regional scale processes may be better represented by the higher resolution available in a regional, rather than global, model.

An ideal region for such a study is the far-eastern Pacific warm pool, where strong intraseasonal variability in the ocean and atmosphere is known to occur, particularly in summer, and to be related to the global MJO (e.g. Kayano and Kousky 1999; Maloney and Hartmann 2000). The east Pacific is also a region of complex topography and oceanographic structure, making use of a regional model particularly useful. Some of the prominent features include strong winds emanating from the gaps in the Central American cordillera (Chelton et al 2000), and high ocean eddy kinetic energy and SST variability offshore of the Central American coast and along 10ºN (Farrar and Weller 2006; Chang 2009).

Statistically significant 50-day peaks in precipitation, wind, and SST can be found in the east Pacific warm pool during boreal summer (Maloney and Esbensen 2003, 2007; Maloney et al. 2008). An important question is to what extent such variability in this region is influenced or enhanced by local processes rather than just being driven by the global MJO. A related question is whether the east Pacific can support strong intraseasonal variability in isolation from the west Pacific.

The main aim of this paper is to investigate the role of air-sea interaction in intraseasonal variability in the eastern Pacific warm pool, using models and observations. We also discuss the role of local circulation-convection feedbacks, and remote forcing from the eastern hemisphere. This study sheds light not only on what regulates intraseasonal variability in the east Pacific, but may also help illuminate what controls intraseasonal variability in the tropics, in general. The structure of the paper is as follows. In section 2 the datasets, models and methods are described. The fidelity of the coupled model to simulate MJO events is discussed in section 3. Section 4 examines the influence of air-sea interaction using regional atmospheric model sensitivity experiments. This is followed by a discussion of the impact of remote forcing and comparison of the results of this paper to previous studies, and, finally, conclusions.

2. Data, Models and methods

2.1 Observations and Reanalysis

The characteristics of convection in the region are deduced from Outgoing Longwave Radiation (OLR) data and a merged precipitation analysis. OLR is obtained from National Oceanic and Atmospheric Administration (NOAA) polar-orbiting satellites, interpolated daily onto a 2.5° by 2.5° grid (Liebmann and Smith 1996). Precipitation is based on the daily TRMM 3B42 rainrate (v5) gridded onto a 1° grid. This dataset combines and calibrates the abundant satellite IR measurements with more accurate passive microwave measurements of precipitation from TRMM. For access to TRMM3B42 see http://daac.gsfc.nasa.gov/precipitation/TRMM_README for details.

Neutral wind vectors at 10 m (Wentz and Smith 1999) are derived from the SeaWinds QuikSCAT scatterometer. SST and column-integrated water vapor from December 1997 is obtained from the TRMM satellite microwave imager (TMI). TMI data is not affected by clouds except under heavy precipitation (Wentz et al 2000) and hence has a significant advantage over infrared radiometers in regions of large cloud cover. The above-mentioned data is obtained from Remote Sensing Systems (www.ssmi.com), processed on a 0.25º grid. For other fields we use National Centers for Environmental Prediction (NCEP)/ National Center for Atmospheric Research (NCAR) daily-mean reanalysis (Kalnay et al. 1996).

2.2 Models

Regional Coupled Model

The International Pacific Research Center (IPRC) Regional Ocean Atmosphere Model (IROAM, Xie et al. 2007) is used for a detailed, high resolution analysis of intraseasonal variability, and for studies of the sensitivity to SST. The atmospheric component is a terrain-following normalized pressure (sigma) coordinate hydrostatic model (Wang et al 2003). It employs a moisture convergence scheme for shallow convection and a modified CAPE closure for deep convection, as well as explicit microphysics. There are 28 vertical levels. Further details and references for the physical schemes can be found in Wang et al. 2003 and Xie et al. 2007. At the lateral boundaries the atmospheric model is nudged towards 4-times daily values of temperature humidity, and wind components from the NCEP/NCAR reanalysis, in a buffer zone 6° wide. This allows observed propagating MJO signals to force the atmospheric model at the boundaries. Including this buffer zone, the model extends from 150°W to 30° W, and from 35°S to 35°N.

The ocean component is the z-coordinate hydrostatic Modular Ocean Model (MOM2) (Pacanowski and Griffies 2000), employing 30 levels, 20 of which are in the upper 400m. The vertical mixing scheme is based on Pacanowski and Philander (1981). We use a constant Laplacian lateral eddy viscosity coefficient of $2 \times 10^{6} cm^{2} s^{-1}$. Surface salinity is restored to Levitus values on a timescale of 30 days. The model covers the Pacific ocean domain from 35°S to 35°N, with sponge layers at the meridional boundaries and walls at the eastern and western coastlines.

A ½°, co-located grid is employed for the ocean and atmosphere, with the ocean salinity and tracer points collocated with atmospheric temperature points. The atmospheric grid is horizontally unstaggered. Xie et al. 2007 (their Fig. 1) describe and illustrate the domain of the complete model system. The fully coupled ocean-atmosphere part of the model covers the Pacific Ocean from 150°W eastwards to the American coastline, and from 35°S to 35°N. In the coupled domain, coupling occurs once per day. The ocean model is spun up with a hindcast from 1991 to the end of 1995 using basin-wide forcing from NCEP/NCAR reanalysis, then the interactive coupling is switched on from 1996 to 2003. Further details and an overview of the model performance can be found in Xie et al. (2007).

<u>Linear Baroclinic Model</u>

The linear response to diabatic heating anomalies is studied using the Linear Baroclinic Model (LBM) of Watanabe and Kimoto (2000). The primitive equations used by the Center for Climate System Research (CCSR) University of Tokyo/National Institute for Environmental Studies (NIES) AGCM, are linearised about a climatological summer (June to September) mean basic state. The sigma-coordinate LBM has 20 vertical levels, contains topography, and is run at T42 resolution. The model is time integrated, and has Newtonian and Rayleigh damping timescales for heat and momentum ranging from 30 days in the free troposphere to 1 day at the top and bottom levels. Chiang et al. 2001 find that results from a similar model do not sensitively depend on the exact thermal damping. Some sensitivity to the Rayleigh damping should however be expected: Wu et al (1999) find that even a relatively weak boundary layer Rayleigh damping ($10day^{-1}$) acts to significantly reduce the boundary layer wind response to heating. Our choice of relatively strong damping rate of $1day^{-1}$ will cause weaker boundary layer winds (see Fig. 11 below) but the free tropospheric winds are not likely to be strongly reduced. The model is forced by a specified diabatic heating anomaly which is constant in time with a specified horizontal and vertical distribution. By 20 days the solution has reached a steady state and these results are shown here. The damping is sufficient to exclude baroclinic instabilities from the simulation.

2.3 Methods

We analyse the years 1998 to 2003, unless specified otherwise. The first two years of interactive coupling (1996-1997) are discarded as being part of the model spin-up process, except where specified. All data is first compiled into pentads before analysis. Frequency spectra are calculated for boreal summer precipitation and SST in the warm pool as in Maloney et al. 2008. Before calculation of the spectra, the climatological seasonal cycle was removed from the data. Spectra were calculated on each individual May-October period during 1998-2003, and then averaged across all six years of data to compute an average spectrum. An expanded May-October period is used to compute spectra to minimize bandwidth, which in our calculations is $(180\ day)^{-1}$. The length of record and two degrees of freedom per spectral estimate produce twelve degrees of freedom for the average spectra. Using the one-day lag autocorrelation and square root of the two-day lag autocorrelation, an estimate of the red noise background spectrum is generated using the formula of Gilman et al. (1963), and then 95% confidence limits on this background spectrum are calculated using the *F*-statistic.

Hilbert transform complex empirical orthogonal function analysis (CEOF analysis, e.g. Barnett 1983; Horel 1984) is conducted during 1998-2003 on modeled June-October intraseasonal precipitation and SST anomalies. Maloney et al. (2008) conducted a CEOF analysis using TRMM precipitation and TMI SST during 1998-2005, to which we will contrast the leading modes of model intraseasonal precipitation and SST variability. For linear regression analysis and variance plots, a temporal 12th order Butterworth filter is applied, to isolate the 20-90 day activity. No spatial filtering is applied, due to the relatively small size of the interactive domain compared to the planetary-scale MJO.

Regional coupled model experiments are performed to analyse the sensitivity of the MJO convection to the surface boundary conditions. Firstly, a control run was performed with a fully interactive coupling (as described in Xie et al. 2007), referred to here as Experiment 1 (Exp. 1). Next, an atmosphere only run was performed (Exp. 2). Here the SST was set to the Reynolds et al. (2002) weekly product (interpolated in time to the timestep of the model)[1]. Third, a further atmosphere-only run was performed with the SST smoothed in time such that the intraseasonal variability of SST is removed in the eastern Pacific warm pool. The smoothing is done with a box-car filter. The averaging time period is spatially weighted, taking a maximum value of 21 pentads in the center of interest (chosen as 90°W, 12°N), decaying in a Gaussian fashion with e-folding widths of 30 ° longitude and 20° latitude. (With this form, the averaging interval reduces to about 1 pentad

[1] The Reynolds et al. 2002 data was used for legacy reasons. It is acknowledged that a product such as TMI SST or the recent high resolution NOAA SST analyses (Reynolds et al. 2007) may have been better choices to capture intraseasonal SST variability (see the Discussion on the strength of SST anomalies).

(i.e. no averaging) close to the domain boundaries, such that an artificial sharp SST gradient near the boundary is avoided. The effect of the smoothing is shown later in Fig. 13c). This experiment is referred to as Exp. 3.

3 MJO in the eastern Pacific: model and observations

3. 1 Summer climatology

In summer a broad warm pool exists in the north-eastern tropical Pacific with SST above 27°C. The precipitation over the ocean is mostly confined to this warm pool region, where convergence occurs in the ITCZ (Fig. 1a,b). South of the ITCZ, the pronounced equatorial cold tongue suppresses convection, whilst in the southern hemisphere tropics and sub-tropics, SST is cooler than at similar latitudes in the north so that atmospheric convection is largely absent during this season. The distribution of mean OLR from NOAA observations (Fig. 1b) closely matches that of the precipitation (Fig. 1a), and shows the presence of deep convection over the warm pool. The wind field at 10m from QuikSCAT (Fig. 1b, vectors) shows the typical trade wind easterly component dominates everywhere except over the warm pool, which exhibits mean westerly winds, and at 10° N the mean 10m zonal winds change sign from easterlies to westerlies at around 125° W (see the mean zonal wind zero contour on Fig. 1b).

The coupled model (IROAM) SST (Fig. 1c) shows a cold tongue and east Pacific warm pool with similar absolute temperatures to those observed from TMI (Fig. 1a). The IROAM rainfall distribution in the Eastern Pacific (Fig. 1c) is close in horizontal structure to the TRMM3B43 observations (Fig. 1a), with a single northern ITCZ, but the magnitude of model precipitation is larger than observations by about a factor of about 1.5 (note the different color bars). As discussed by Xie et al. (2007) with regard to the annual mean climatology, this increase may be related to higher wind speeds and evaporation in IROAM. Likewise, the OLR structure is comparable between model (Fig. 1d) and NOAA satellite OLR data (Fig. 1b), except for a general bias of higher OLR in the ITCZ in the model by about $20Wm^{-2}$ (linked to a negative bias in cloud cover/height in IROAM, Xie et al. 2007). Similar to the observations, the mean zonal winds are westerly over the warm pool in the model (Fig. 1d).

The climatological mean ocean mixed layer depth in the model is 20m to 30m in the warm pool region (Fig. 1e, color): this may be compared with an analysis of in-situ observations by Fiedler and Talley (2006) which showed values of 20m to 40m. The depth of the model 20º C isotherm (a representative thermocline value) is between 40m and 70m in the warm pool (Fig. 1f, color), with a minimum value of 30-40m centered near 10º N, 90º W (the Costa Rica Dome, Wyrtki 1964; Kessler 2002; Xie et al. 2005), and again these values are consistent with those found in observations (Fiedler and Talley 2006).

3. 2 MJO amplitude and phase relative to observations

Intraseasonal wind variability, as measured by the standard deviation of filtered zonal wind at 850hPa, from all months, is comparable in the IROAM model and the NCEP/NCAR reanalysis (Fig. 2). In particular, a local maximum observed in the latitude band 5° to 20°N, and longitudes 120°W to Central America, is prominent in the observations and model, with anamplitude of around $3ms^{-1}$. The skill of the regional model in reproducing the observed MJO zonal wind signal is assessed by defining a zonal wind index, simply the average of the filtered 850hPa zonal wind between 10° and 15° N, 130° and 100°W (an area of large variance), and then lag correlating the model zonal wind index with the observed index. From Fig. 3 it can be seen that the correlation is almost 0.8 at zero lag and reaches -0.5 at about 20-25 days before or after. These results are highly significant at 99% using the student *t*-statistic: assuming that each 50 days (about the period of an MJO event) is an independent sample, about 44 independent samples are found over the entire record[2].

A somewhat tougher test of the model is to compare the convection characteristics with observations. Fig. 4a, b shows the standard deviation of filtered OLR for IROAM and from observations. Here only the summer months (June to September) have been considered, as this is the season of strongest Eastern Pacific MJO convective variability (Maloney and Esbensen 2003). The overall amplitude of OLR variability in the ITCZ is similar in model and NOAA data, peaking at about $20Wm^{-2}$ (Fig. 4a, b). However, some spatial differences exist in the OLR variability: the NOAA data shows a maximum adjacent to the Pacific coast of southern Mexico (Fig. 4a), whereas the model places the maximum further offshore, west of 100°W (Fig. 4b).

Intraseasonal precipitation variance maps (not shown) have a similar distribution to the OLR variance, but, as with the climatological mean (Fig. 1), the amplitude of the model precipitation variability is about 1.5 times the TRMM observations. More information regarding the nature of the variability can be gleaned from frequency spectra. The spectrum of boreal summer model unfiltered precipitation averaged over a 10^o x 10^o box centered at 15.5^oN, 104.5^oW indicates a significant spectral peak near 50 day period (Figure 5a),

[2] This is a conservative and strict estimate of independent samples – it can also be argued that an independent sample has the duration of the wet phase of the MJO which is typically less than half of the total MJO period.

similar to observations from TRMM (Fig. 5b, from Maloney et al. 2008). Thus, the regional model captures intraseasonal precipitation variability in the heart of the warm pool with a similar dominant timescale to observations..

As with the 850 hPa zonal wind, a lag correlation was performed between the 20-90 day filtered IROAM OLR and the corresponding NOAA OLR. (Here a different box-average was chosen for the OLR index than that used for the zonal wind since OLR anomalies change sign across 120° W. The OLR averaging box was chosen to be 10° to 20°N, 110° to 100°W.) Over all seasons there is an instantaneous correlation of 0.6, again significant at 99%, and a negative correlation of -0.3 20 days before and after (Fig. 6a, dashed line). Similar correlations were found when only the summer was considered, but here there were fewer independent samples to achieve significance. For comparison, the autocorrelations of NOAA OLR (thick solid line) and of IROAM OLR (dot-dash line) are also displayed (Fig. 6a): these curves suggest that there is a small difference in the MJO period between model and observations: the first trough being at 20 days in NOAA and 15 days in IROAM. We note that the global MJO index of Maloney and Hartmann (2000) is correlated at 0.6 with observed intraseasonal precipitation in our averaging region (Maloney et al. 2008), suggesting that a substantial portion of the intraseasonal variability there is explained by the MJO. By comparison, the global MJO index is correlated with regional west Pacific and Indian Ocean OLR by at most 0.7 during boreal summer and winter. As indicated in Figure 6, model intraseasonal convection in the warm pool is in phase with that from observations, partly due to forcing of the regional coupled model at the boundaries, in this case associated with MJO-induced dynamical signals propagating into the domain, discussed further in section 5.

A local complex EOF analysis (CEOF, introduced in section 2.3) is used to further examine the phase properties of the leading mode of intraseasonal precipitation variability in this region. The spatial amplitude, local variance explained, and spatial phase for the leading CEOF of modeled intraseasonal precipitation is shown in Figure 7 (right panels). This leading mode explains 19% of the total variance of precipitation over the domain shown, and is separable using the criterion of North et al. (1982) from the second and third modes (which explain 10% and 8% of the variance, respectively). For comparison, the observed first mode explained 26% of the variance (Maloney et al. 2008), whilst the amplitude structure, spatial phase and propagation characteristics of the leading mode are very close in model (Figure 7d, e, f) and observations (Fig. 7a, b, c, taken from Maloney et al. 2008), with high amplitude across the ITCZ and east Pacific warm pool. The local variance explained by this leading model CEOF is slightly smaller than observations over the warm pool, peaking near 0.5 to the south of Mexico, whereas observed local variance explained approaches 0.7. (Note that although there is large variance explained over the cold tongue in the model (Fig. 7d) that is not observed (Fig. 7b), the amplitude in this region is negligible (Fig. 7d)).

In both model and observations the spatial phase of precipitation varies little in the center of warm pool to the south of Mexico, albeit with suggestions of slow northward propagation when combined with increasing temporal phase (Figure 7c, f). Precipitation in these central warm pool regions just south of Mexico lags precipitation along 8^{o}N to the east of 120^{o}W by about 100 degrees of phase (about 2 weeks for a 50-day cycle). Also similar to observed, precipitation to the west of 120^{o}W leads that in the warm pool by 125-150 degrees of phase.

3.3 Dynamic and convective structure of MJO in Eastern Pacific

The time evolution of typical MJO events in summer in observations and model is computed by lag regression. As above, the index used in the regression analysis is defined as the negative of OLR anomalies averaged in a box 10° to 20°N, 110° to 100°W (shown in Figs. 8c, 9c). It is noted that local and global indices of intraseasonal activity produce similar results (e.g. Maloney and Hartmann 2000, 2001). Lag regression plots of OLR and 850hPa winds from observations are shown in Fig 8. Associated with convection at lag 0 are strong westerlies at 850hPa extending from 10° S to 20° N, and positive vorticity to the north and west (Fig. 8c). During the dry phase in the far eastern Pacific (e.g. at -20 days and +20 days, Figs. 8a,e) there are easterly wind anomalies and anticyclonic vorticity to the north and west. These features bear some similarities with the Kelvin wave/Rossby wave couplet of Gill (1980) for a source in the northern hemisphere, but the easterly inflow of the Kelvin wave response to heating to the east of convection appears to be nearly absent in the observed circulation (Fig. 8c). The correspondence of convective anomalies in the eastern Pacific warm pool with westerly wind anomalies and dry anomalies with easterly winds is similar to the composites of Maloney and Hartmann (2000) based on a global zonal wind MJO index.

The temporal evolution of OLR in the IROAM model[3] (Fig. 9) exhibits very similar, albeit weaker[4], structure to observations, including the zonal wind/convection relationship, and a change of sign of the OLR anomaly across 120°W at zero lag. Plots of

[3] Note that now the model data is regressed onto an OLR index derived from the model data, so as to display the interrelationship between model fields more clearly. (For reference Figs 6 and 10 show the model-observation comparison)

[4] The slightly weaker amplitudes of the anomalies in the model at non-zero lags, compared to those in observations, are not due solely to a weaker variance (as can be seen by noting that the OLR variance in the model is greater than observed in some locations, (Fig. 4a,b), but probably also due to a weaker correlation between distant points and the index box.

OLR lag correlation vs longitude (Fig. 10a, averaged over the latitude band 10° to 20°N) reveal that instead of a smooth propagation of convection from west to east in boreal summer, there is instead a very rapid change of phase around 120°W. Northward propagation is also apparent in the lag regressions averaged between 110°W and 100°W (Fig. 10b), consistent with the observational analysis of Maloney et al. (2008) and with the CEOF analysis shown above. This northward propagation, examined extensively in Jiang and Waliser (2008), parallels the poleward summertime propagation manifested in other monsoon systems, especially the Asian monsoon (e.g. Wang and Xie 1998). .

The wind fields associated with the MJO convection in observations and model may be interpreted with the aid of a Linear Baroclinic Model (LBM, section 2.2). The diabatic heating input for the LBM is estimated from the precipitation patterns from TRMM and IROAM, regressed onto the OLR index, at zero lag. These precipitation patterns are not shown, but are spatially reasonably similar to the OLR distributions (Fig. 8c, 9c), with the maximum precipitation anomaly being ~0.15 mm day^{-1}/Wm^{-2} in the observations Based on these patterns, a maximum diabatic heating equivalent to 0.15 mm day^{-1} is prescribed, i.e. the heating that is equivalent to 1Wm^{-2} of OLR variability. The horizontal structure is an idealized ellipse based on the observed convection east of 110°W (Fig. 11a)[5].

For the vertical structure, we use a sinusoidal profile (Fig. 11b), which leads to a diabatic heating that peaks at 0.06Kday^{-1} at σ=0.5 in the center of the ellipse. This scaling allows direct comparison with Figs. 8-10. (To convert to the heating and response due to a typical MJO, given the units of the regression coefficient, multiply the values by about 20,

[5] Note that if we added a second ellipse of opposite sign to represent the weak and less-broad negative anomaly west of 110° W, the results are not significantly different, due to the smaller magnitude and spatial area of this anomaly.

the maximum standard deviation of OLR (in Wm^{-2}: see Fig. 4). The vertical structure is that of a highly idealized first baroclinic normal mode for a system with constant buoyancy frequency (Gill 1980). Other possible choices of profiles include that simulated by IROAM, and those from various observational products. For the former, diabatic heating data was not saved from the model, but investigation of the vertical velocity data showed that a low level maximum (800hPa) was present in some parts of the Eastern Pacific ITCZ in time mean fields (not shown). For the latter, observations are rather limited, but Lin et al. (2004) show slightly elevated heating anomalies (with a maximum between 400 and 500hPa) due to the MJO in the western Pacific warm pool, whilst Thompson et al. (1979) show a lower maximum at 700hPa from observations over the Atlantic ITCZ, and Back and Bretherton (2006) infer mean heating profiles with low-level maxima at 800hPa or below from ERA40 data in the east Pacific ITCZ. The vertical structure of heating is very important, as the potential vorticity tendency is related to vertical gradients of potential temperature tendency (Mapes, pers. comm.. 2007), and low level heating maxima may project onto higher modes of the system with potentially stronger low level winds (Wu et al. 2000; Chiang et al 2001). Thus, it is acknowledged that the following results present an idealized scenario that only qualitatively illustrate the impact of heating on the low-level circulation.

The heating results in a band of anomalous westerlies between 5° and 20°N at 1000hPa (Fig. 11c) and 850hPa (Fig. 11d). The zero contour of the climatological summer zonal wind is overlaid on Fig. 11c for reference: within this contour the anomalous westerlies would enhance the zonal wind component, and as both the anomalous and mean meridional wind components are mostly southerly in this region, (Fig 1b, 11c), the wind speed, and thus the evaporation (see section 4), would be increased under the anomalous winds. Further, the background low level convergence would be enhanced by the convergence of the 1000mb anomalous flow (Fig. 11c). The wind response fields are similar in structure to those observed and seen in IROAM (Figs 8c, 9c) but are weaker in magnitude in the LBM (by approximately a factor of two), whereas the convergence in the LBM is weaker by a factor of three. The relatively small anomalies near the surface produced by the LBM may be a result of the reasonably strong boundary layer friction employed here (see section 2.2). Another notable difference is that the reanalysis and IROAM winds anomalies extend further south than in the LBM, crossing the equator and suggesting a possible Kelvin wave component as discussed in the next section.

To summarise this section, the observations and IROAM model lower tropospheric fields are mostly consistent with those expected from the linear response to prescribed heating, but with a larger amplitude. The difference in amplitudes may arise from feedbacks between the circulation and convection (e.g. Zebiak 1986) and other non-linearities not included in the LBM, or the influence of remote forcing (see below). The LBM analysis shows that wind speeds will be increased in the zone of mean westerlies and decreased in the mean easterly region (e.g. refer to Figure 1), thus allowing for the potential of surface evaporation flux feedback effects whilst frictional convergence induced by the heating could also provide a positive feedback.

3.4 Remote forcing of intraseasonal convection

The high correlation between intraseasonal precipitation variability in the east Pacific warm pool and the global MJO (Maloney et al. 2008) indicates that remote forcing is likely important for producing intraseasonal variability in the east Pacific warm pool. Where does the remote forcing originate from, how does it propagate, and why is the largest effect of the MJO outside of the Indo-Pacific region found in the eastern Pacific warm pool?

Hovmöller diagrams provide some insight into the influence of intraseasonal oscillations propagating into the domain. Figure 12 shows the time and longitude variation of filtered 850 hPa zonal wind (U850), averaged between 10ºS and 10ºN, and of filtered OLR, averaged between 10º and 20ºN, for the summer of 2002, a year of reasonably strong MJO variability. (The latitudes of averaging are chosen based on the relative equatorial symmetry of the global MJO zonal wind anomaly, and the asymmetric nature of the local convection.)

There are clear signals of U850 anomalies at the western boundary of the model (150ºW) (Fig. 12b, contours) that are forced by MJO convection in the west Pacific. The BCs for zonal wind are from the NCEP/NCAR reanalysis, shown in full in Fig. 12a (contours). (By design of the BCs, the zonal wind anomalies at the far west and far east of Fig. 12a and b are nearly identical.) There is a weaker matching of observed and model OLR anomalies at the boundaries (Fig. 12a, b, color). This is partly because OLR is not a prognosed variable passed into the model at the boundaries: specific humidity is the only moisture variable that is passed, so it may take some time for convection to initiate, given the right conditions.. There is a rather good matching of OLR in the interior of the model domain to the corresponding observations (Fig. 12a, b), which confirms the linear regression analysis shown above (Fig. 8, 9). The OLR anomalies are generally stronger in the domain interior than at the boundaries (in both model and observations).

Once convection is initiated in the off-equatorial east Pacific by the equatorial propagating wind signal, the strongest wind anomalies to the east of 240^{o}E also move off the equator, as can be seen in Figures 8 and 9. These results show that the boundary forcing from zonal winds is important to the local intraseasonal variability, and since the east Pacific warm pool is a large spatial area of warm SST associated with decreased stability, it supports large-scale anomalies in convection and the circulation.

Global maps of the OLR anomaly during the period of enhanced convection in the Eastern Pacific warm pool show a large region of suppressed convection centered on the western equatorial Pacific/Maritime Continent region associated with the MJO (e.g. Maloney and Hartmann 2000a their Fig. 3, top panel)[6]. Associated with the suppressed eastern Hemisphere convection are westerly anomalies across much of the equatorial Pacific, typical of an equatorial Kelvin wave response to a negative heating anomaly.

It is possible that the Eastern Pacific reinitiation of convection is related to the suppression of convection in the eastern hemisphere. This would lead to cool tropospheric temperature anomalies, anomalous equatorial surface westerlies and a high pressure anomaly that propagates eastward, at the fast propagation speed of a dry Kelvin wave. We note that it would take just 3 days for such a Kelvin wave to cross the Pacific, essentially instantaneous communication with the Eastern Pacific in pentad data. Figure 12 shows evidence of such fast Kelvin wave propagation. Consequently the convection in the Eastern Pacific may be initiated by Ekman convergence on the north-eastward flank of the dry Kelvin wave as it propagates into the region**.** These findings are supported by the work of Maloney and Esbensen (2007), who showed a substantial meridional convergence

[6] Further, Wang et al (2006) show a "see-saw" oscillation between convection in the Bay of Bengal and the eastern North Pacific region investigated here.

signal in QuikSCAT data associated with the initiation of east Pacific MJO-related convection events. (A related mechanism was proposed by Xie et al. 2009 for the remote influence of the Indian Ocean on the generation of the subtropical anticyclonic anomaly in the north-west Pacific in the summer after El-Nino peaks. There it was proposed that Ekman divergence on the northern flank of an eastward propagating low pressure Kelvin wave, together with feedbacks between the circulation and convection, acted to maintain the anticyclone.)

Other studies have found that intraseasonal variability in the Tropics preferentially occurs in regions of mean low-level westerly winds, where westerly wind anomalies associated with positive precipitation anomalies can add constructively to the mean flow and cause anomalously strong surface latent heat fluxes (Sobel et al. 2010). The mean flow in the east Pacific warm pool is westerly during boreal summer, and propagation of westerly anomalies into the region would enhance surface fluxes and possibly initiate convection.

4. Surface fluxes and air-sea interaction processes in the MJO

Previous studies have suggested a role for surface flux anomalies in supporting MJO convective variability, either through their impact on SST (e.g. Waliser et al. 1999), or through their direct impact on the atmospheric moisture and energy budgets (e.g. Raymond 2001; Sobel et al. 2008). In this section, the importance of these processes are explored in the regional model through modeling experiments both in a coupled mode, and in an atmosphere only mode with different SST settings.

4.1 SST variability in model and observations.

The Eastern tropical Pacific contains ocean mesoscale variability on a range of timescales. Tropical Instability Waves contribute to large SST anomalies contained within 5º of the equator, with periods between about 15 and 30 days (Legeckis 1977). In addition strong ocean mesoscale eddy activity on intraseasonal timescales has been observed offshore of the Tehuantepec and Papagayo gaps (Liang et al 2009, Chang 2009) and out along 10ºN (Farrar and Weller (2006). Both gap wind forcing (McCreary et al. 1989) and mean flow instabilities are important for the eddy generation (Chang 2009), with instability of coastal Kelvin waves playing a role off Papagayo (Zamudio et al 2006). Along 10ºN, baroclinic instability of the North Equatorial Current (Farrar and Weller 2006) energizes eddies. The local maxima in standard deviation of SST seen in Fig. 13b close to the equator and close to the Costa Rica dome (90ºW, 10ºN) are signatures of the mesoscale eddy variability discussed above.

This mesoscale variability can have intraseasonal timescales, but does not have the large spatial scale of the MJO SST signal. For example, Tropical Instability Waves typically have wavelengths about 1000km (Legeckis 1977). In contrast Maloney et al. (2008) used coherence and complex EOF analysis to show intraseasonal TRMM SST anomalies that are coherent across the east Pacific warm pool, and dominated by spatial scales the same size as the warm pool itself. These warm pool SSTs are correlated at greater than 0.7 with an MJO index constructed using data from across the tropics having maximum variance centers in the Indian and west Pacific Ocean.

The standard deviation of 20-90 day SST anomalies in the coupled model (Fig. 13a) is between 0.2° and 0.4℃ in the region of greatest OLR variability (Fig. 4b), comparable to that found in Reynolds et al. SST (shown in Fig. 13b), but weaker than that found in TRMM TMI (Maloney et al. 2008). These values are also comparable with the typical temperature anomalies of 1/3° C in the Indian and western Pacific Oceans, as summarized by Hendon (2005). The coupled run has somewhat larger 20-90 day SST variability than the Reynolds et al. SST in the Equatorial Front and Tropical Instability Wave latitudes (centered around 2^{o}N), and somewhat less variability off the coast of Mexico north of 15°N (see the difference field in Fig 13d), but otherwise the differences are less than 0.1°C over much of the warm pool convection region.

In the far-eastern tropical Pacific warm pool, a significant 50-day spectral peak in SST is found by Maloney et al. 2008 (reproduced in Fig. 5d). However, such a peak is not found in the model SST, which instead shows an essentially red power spectrum (Fig. 5c). Further, the leading CEOF of intraseasonal SST in the model shows some significant differences from observations, particularly in spatial distribution, having a local minimum of amplitude around 8-10ºN (Fig. 14d), where the amplitude of the observed CEOF of SST is large (Fig. 14a). Although temporal phase and amplitude of the leading CEOF of model precipitation and SST indicate that these CEOFs are correlated at 0.8, and thus appear to be coupled, the very different spatial structures of precipitation and SST make it unlikely that intraseasonal SST anomalies provide important feedbacks onto model intraseasonal precipitation variability.

The fact that the structure of model OLR variability is comparable to observations, but the model SST variability is not, suggests that either the intraseasonal SST anomalies do not play an essential role in modulating east Pacific precipitation variability, or that the model convective variability is too much dominated by the lateral boundary forcing (i.e. the model dynamics exaggerate the response within the domain to the boundary signal) so that SST effects are overwhelmed. In the following subsections some testing of these possibilities is done by examining the role of SST in the surface fluxes, and by performing sensitivity experiments to SST distributions.

4.2 Sensitivity to SST in atmosphere-only experiments

We now compare the OLR variability in the coupled run (Exp. 1) to that in the atmosphere-only sensitivity runs (Exp. 2 and Exp. 3) introduced in section 2.3. As discussed above, the differences in 20-90 day SST variability between the coupled run and Exp. 2, are by definition the same as the differences with Reynolds et al. (2002) SST (the difference field is shown in Fig. 13d). In Exp. 3, the effect of the smoothing the SST can be clearly seen in Fig. 13c, with essentially all intraseasonal SST variability removed in the East Pacific Warm Pool.

It is important to note that differences exist in the mean state produced by these runs, as well in the intraseasonal variability. Reproduced in Fig. 4e (contours) is the climatological summer mean SST difference between Exp. 1 and Exp. 2. Differences reach up to +/- 1°C: in particular in the warm pool north of 15°N the SST is warmer in the coupled run. It is generally cooler in the coupled run to the south of 15°N, except in the upwelling region offshore of Peru. These changes in mean SST lead to corresponding changes in mean precipitation and OLR (not shown), such that there is more (less) precipitation where the coupled model SST is warmer (cooler). The differences of OLR intraseasonal variability show a similar pattern, with greater (reduced) OLR variability in the coupled model relative to the atmosphere-only model when the mean SST is warmer (cooler). Thus, in a comparison between Exp. 1 and Exp. 2, it will be difficult to determine whether the changes in convective variability are due to the change in the mean SST, or due to the modification of intraseasonal convection by coupling. (This point was recognised by Waliser et al. 1999, who employed an anomaly-coupled run to remove this effect, and by Innes et al. (2003), who found that the MJO was better simulated in a coupled model when flux correction was employed to constrain the background state). These differences in mean state do not apply when comparing the atmosphere-only runs Exp. 2 and Exp. 3, for which the mean SST is the same by design, and the mean precipitation fields are also very similar (not shown). It follows that comparison of these two simulations will show changes that are solely due to the presence or otherwise of intraseasonal SST variability.

The OLR variability in the atmosphere-only run adjacent to the Pacific coast of southern Mexico is closer to observations in this region than the coupled model (compare Fig. 4a, b, c), and part of the reason for this seems to be the bias in mean SST in the coupled model relative to observations (Fig 4e contours).

In contrast to the systematic differences in intraseasonal OLR variability between Exp. 1 and Exp. 2, differences between the atmosphere-only run with smooth SST (Exp. 3, Fig 4d), and the atmosphere-only case with no smoothing (Exp. 2, Fig. 4c) are patchy in nature (Fig. 4f). There is no evidence of a systematic reduction in OLR variability when the SST variability is removed.

The lag correlations between the OLR in the sensitivity runs and the NOAA OLR (Fig. 6b) reveal that Exp. 2 has a slightly lower instantaneous correlation (0.54) than Exp. 1 (0.6), and Exp. 3 has the lowest correlation (0.5). Thus, although the spatial distribution of the OLR variability is somewhat better in the atmosphere-only run than in the coupled run, and there is no systematic difference in OLR variability between Exp. 2 and Exp. 3, there does seem to be a slight improvement in correlation with observations when coupling and SST variability is included.

4.3 Surface latent heat flux: the contribution of wind speed and SST anomalies

In the IROAM coupled model, evaporation anomalies are almost in antiphase with the OLR (Fig. 15a, c), such that more evaporation occurs in conjunction with convection. This is consistent with the observational analysis for this region of Maloney and Kiehl (2002b), and Maloney and Esbensen (2007). The corresponding regression maps of scalar wind speed are spatially similar to that of the surface latent heat flux, except that there is a notable change of sign west of 120°W (Fig. 16a, b). This change of sign (due to the fact that the zonal wind anomalies cross the zero point of the mean zonal wind) is reminiscent of the dipole in convection. It may be noted from Fig. 15 that there is no corresponding dipole in latent heat flux. However, when the latent heat flux is regressed instead on OLR variability in an index box located in the warm pool west of 120°W, a high (negative) correlation was found between evaporation and OLR in that region (not shown). This suggests that when there is convection east of 120°W, which is accompanied with positive OLR anomalies west of 120°W (Fig. 8c, 9c), there should be negative evaporation anomalies west of 120°W, which is not seen in Fig. 15a, b, e, and the reason for this may be a weakness of the regression technique, with small correlations between latent heat flux in one dipole and OLR variability in the other.

The corresponding temporal variations of SST in the coupled model (Fig. 17a,b) show that the SST is almost in quadrature with OLR, such that warm SST tends to precede convection by 2-3 pentads, and cool SST lags convection by about 2 pentads. These results are reasonably consistent with the observational analysis of Hendon and Glick (1997) for the Indian and western Pacific Oceans, and Maloney and Kiehl 2002b, Maloney et al. 2008 for the Eastern Pacific summer warm pool. They are also consistent with the expected response of SST to increased evaporation (and possibly entrainment) under the strong winds associated with convection, as well as the reduction of solar insolation due to increased clouds.

More information on the sensitivity to SST is given by regression plots for SST and OLR in Exp. 2 (Fig. 17c,d) which may be compared with the coupled run discussed above (Fig 17a, b). The atmosphere-only run produces an SST-OLR relationship which is slightly altered relative to the quadrature of the coupled run, such that the SST anomalies appear about 1 pentad later (compare Fig. 17b,d), and are thus shifted to closer in phase to the negative OLR (compare e.g. Figs. 17a, c). This is a typical one-way response of the atmosphere to SST, because in this sensitivity experiment the atmosphere is not allowed to modify the SST via short wave fluxes or evaporation, as would occur in the coupled run, which would lead to cooling under convection.

The regression plots for latent heating, wind speed and SST (Figs. 15-17) suggest that SST is not having a significant effect on the evaporation, as summarized in the following two points. Firstly, in the fully coupled run the SST is almost in quadrature with (orthogonal to) evaporation, so that the SST anomalies could just be a passive response to the surface heat flux. Secondly, the evaporation for the no-SST variability case Exp.3 (Fig.

15e,f) is similar to that of Exp. 1 and Exp. 2 (Fig 15a,b) and appears to be more governed by the wind speed variability which is qualitatively similar in all cases (not shown, but wind vector anomalies are shown in Figs. 15a, b, e)).

A simple scaling analysis is helpful to estimate the relative importance of SST and wind speed fluctuations to the evaporation anomalies. Writing the bulk flux formulation of evaporation E in the standard form

$$E = \rho L C_E U \left(q_s(SST) - q(T_a) \right) \qquad (1)$$

where U and T_a are near surface (typically 10m) wind speed and surface air temperature respectively, q is humidity, q_s is saturation specific humidity, L the latent heat of vaporization, ρ the air density and C_E the 10m turbulent exchange coefficient for latent heating, then the change in evaporation due to a change in wind speed (ΔU) and that due to a change in SST (ΔSST) is given by

$$\Delta E = \rho L C_E \left(U - \Delta U \right)\left(q_s(SST + \Delta SST) - q(T_a + \Delta T_a) \right)$$

where it is seen that the air temperature will also respond by an amount ΔT_a. One way to approximate the relative roles of SST and wind speed in this expression is to assume a constant relative humidity (RH) and constant sea minus air temperature difference. Then the humidity difference in (1) is given by

$$q_s(SST) - q(T_a) = q_s(SST) - RH q_s(T_a)$$

Linearising the Clausius-Clapeyron relationship about the SST, so that $\partial q_s/\partial T = K$, a constant, and $q_s(T_a) = q_s(SST) + K(T_a - SST)$, it is easily shown that

$$\Delta E = \Delta E_W + \Delta E_{SST} + \Delta U(1 - RH) K \Delta T \qquad (2)$$

where

$$\Delta E_W = \rho L C_E \Delta U \{(1 - RH) q_s(SST) + RH.K(SST - T_a)\}$$
$$\Delta E_{SST} = \rho L C_E U (1 - RH)(K \Delta SST)$$

are the wind and SST contributions respectively and the second-order last term in (2) is neglected.

We can then estimate the change in evaporation from the IROAM model results, noting that SST anomalies reach up to ~0.6×10^{-2} K per Wm^{-2} (Fig 17) whilst wind speed anomalies are around 0.03 ms^{-1} per Wm^{-2} (Fig.16). Consider now a 10 Wm^{-2} anomaly of OLR, which would lead to a change of SST (ΔSST) of 0.06ºC and a wind speed change (ΔU) of 0.3 ms^{-1}. Assume also a background SST of 27ºC, and a mean wind speed U of 6ms^{-1}. Table 1 lists the resulting values of ΔE_W and ΔE_{SST} for some selected values of RH and SST-Ta. It can be seen that for a wide range of possible values, the wind contribution is an order of magnitude larger than the SST contribution. (Typical values of RH and SST-T_a in our region of interest are 75% (see Fig. 1f) and 1.5 ºC (see Fig. 1e) respectively, where the wind contribution is 7.0 Wm^{-2} and the SST contribution is 0.26 Wm^{-2} from Table 1. These values do not add up to the original 10 Wm^{-2} because of the approximations of constant RH and SST-T_a, as well as approximate linear regression fit.

The above scaling was based on the typical IROAM SST and wind speed anomalies, but it should be noted that similar magnitudes of anomalies were seen in NCEP/NCAR reanalysis winds and Reynolds et al. SST. However, recent findings from satellite scatterometer and microwave imager data suggest that the typical anomalies are somewhat larger, around 1ms^{-1} for wind speed (Maloney and Esbensen 2007) and 0.5ºC for SST (Maloney et al 2008.), derived using a intraseasonal composite method. Again, this gives rise to much larger values of wind contribution to evaporation (19.6Wm^{-2}) compared to the SST contribution (1.8Wm^{-2}). This shows that SST variability does not have a large impact on east Pacific intraseasonal evaporation, and the coupled model results further suggest that the coupling does not affect the intraseasonal convection. In contrast the mean SST is clearly important, presumably since a larger time-mean SST would foster more convective instability and support stronger convective events, even if the SST variability was unchanged.

4.4 SST and the influence on low level convergence

The above analysis has focused on the role of SST and coupling in modifying the surface latent heat flux. Another possible avenue by which the SST can affect the atmospheric convection is via moisture convergence (Lindzen and Nigam 1987; Waliser et al. 1999). In this proposed mechanism, air temperature anomalies in the boundary layer, which are correlated with SST anomalies, induce hydrostatic pressure gradients which drive winds and convergence. This possibility is investigated by examining the wind convergence at 10 m, which is used here as a proxy for the low level moisture convergence.

In the coupled run (Exp. 1) at lag zero the low level convergence hugs the Pacific coast (Fig. 18a) whereas the 850hPa convergence underlies the main convective center (Fig. 18c), the latter being expected for a first baroclinic mode in the free troposphere. Hovmöller diagrams confirm that the 10m convergence leads the OLR anomaly and the 850hPa convergence by about 1-2 pentads, particularly in the longitude band of 110ºW to 100ºW (compare Figs. 18b, d). In the atmosphere-only case (Exp. 2), a similar spatial pattern of low level convergence was obtained, but some weakening (relative to the coupled run) was seen (not shown). However for the uncoupled and smooth SST run (Exp.

3), there was very little difference in surface convergence relative to Exp. 1, (compare Figs 18e, f with Figs. 18a, b), indicating that SST variability is not significantly affecting the low level convergence (compare Figs. 18e, f with Figs. 18a, c).

By comparison, Maloney and Kiehl (2002b) also found a small direct contribution of SST anomalies to surface convergence (about 10% of the observed total). However they speculated that this small convergence anomaly, (which preceeded the main convection by about 2 pentads), could trigger initial convection which would then enhance the convergence anomaly via the mechanisms demonstrated by the LBM, i.e. convection-circulation feedbacks. The comparison in this paper of simulations with SST anomalies (Exp. 2) vs those without (Exp. 3) would seem to suggest that the SST-induced moisture convergence and the associated feedbacks are not having a large effect: rather, the intraseasonal anomalies in low level convergence in the model, which lead free tropospheric convergence by 1 to 2 pentads, are primarily driven by the atmospheric heating (Gill 1980) and the boundary layer frictional effects (Wang and Rui 1990; Wang 2005). However it may be argued that larger amplitude SST anomalies would lead to a more significant effect (see the related Discussion below).

5. Discussion

In this paper it has been shown that the coupled model variability exhibits a significant correlation with the observed intraseasonal zonal winds and OLR, such that the phase of zonal wind and OLR anomalies is very close (within a pentad) between the model and observations. Obtaining skill in simulating both amplitude and phase relies on a balance between the role of boundary forcing and the local convection-circulation and ocean-atmosphere feedbacks. If the local processes are too strong, the skill may be reduced, particularly for phase, as the boundary conditions lose importance. Conversely, weak local feedbacks would likely lead to small amplitude variability within the domain. Considering the results of the regional coupled model, linear baroclinic model and observations together, it appears that the intraseasonal variability in the eastern Pacific warm pool is governed by the global MJO and the feedback between convection and circulation, but has a weaker dependence on ocean-atmosphere coupling.

Intraseasonal OLR variability in the coupled model had slightly improved correlation with observed values when compared to the atmosphere-only sensitivity runs (Fig. 6b). However, the phasing of the peak OLR in the sensitivity runs is close to that in the coupled run and in the observations, and the amplitude of OLR variability is not systematically reduced when the SST variability is smoothed out (Fig. 4). These results suggest that the intraseasonal variability of SST in the east Pacific warm pool is not making a large impact on the intraseasonal convection in this model and this region. This leads to the question of why coupling has such a small effect, whereas most previous studies such as Flatau et al 1997, Waliser et al 1999, and Maloney and Kiehl 2000b found that coupling improves the MJO simulation? One possibility is the regional nature of the model, which contrasts with the previous papers that typically consider global models. In a global model, sensitivity to SST in a given region can influence the global MJO and subsequently affect the MJO signal coming into that region: whereas in our regional model this feedback is not possible. Another possibility is that the slab mixed layer of constant depth utilised by e.g. Waliser et al (1999) and Maloney and Kiehl (2000a) does not provide a realistic simulation of the ocean, e.g. by not capturing the observed inhomogeneity of background mixed layer depth (Fig. 1e) or by not allowing mixed layer depth to respond to surface stress and flux variability. More recently, another aspect of air-sea interaction has been implicated for improving simulations of the MJO: Woolnough et al (2007) find that a good representation of the near surface diurnal variability enhances MJO predictability. Our model does not capture diurnal variability due to the daily coupling interval.

The SST anomalies produced by the coupled model are comparable to those seen in the SST analysis of Reynolds et al. (2002) but weaker than those inferred from TMI data (Maloney et al. 2008). Our assumption is that the response to coupling is linear, but it may be possible that nonlinear effects become important when SST anomalies become large (i.e. larger than those seen in the coupled model Exp. 1, and also larger than those used in Exp. 2). The exponential form of the Clausius-Clapeyron equation is one possible source of nonlinearity (which we approximated to linear in section 4.3). Further, the mean SST in the coupled model is lower than that in observations (Fig. 4e), which would act to further reduce the absolute value of SST in the warm SST phase of the model compared to observations and weaken the response of surface fluxes anomalies to SST variations. It may be possible that at higher values of absolute SST, feedbacks between ocean and atmosphere become more significant. Thus, for studies of the MJO it is important that modeling efforts continue with a goal of obtaining more realistic SST in coupled models and atmosphere-only models.

A question which arises from the study is how much of the intraseasonal variability in this region is due to global MJO, and how much due to other processes. OLR variability in the east Pacifc warm pool is highly correlated with an index of the global MJO, as is the intraseasonal SST variability, both of which are dominated by spatial structures of the same size as the east Pacific warm pool itself (Maloney et al 2008). Other processes, such as strong gap winds and the high ocean mesoscale variability mentioned in the introduction contribute locally to SST variability but are not likely to have a direct effect on intraseasonal convective variability on the scale of the warm pool (although they can affect precipitation on small scales, e.g. Wijesekera et al. 2005). The gap winds have decorrelation timescales of around a week or less (see Chelton et al. 2000, their Fig. 14, thin lines), much shorter than the intraseasonal timescales of interest.

The above discussion should not exclude the possibility of the interaction between intraseasonal variability and other phenomena in the region. Maloney and Esbensen (2007) show that the low level zonal wind anomalies due to the global MJO modulate the gap winds in the Gulf of Tehuantepec and Papagayo, and thus the MJO itself may influence the nature of ocean eddy variability in this region. In addition, there appears to be a connection between MJO variability and the mid-summer drought over Central America and Mexico (Magana et al. 1999, Small et al. 2007). Recent unpublished work by the authors suggests that in some years, the timing and magnitude of MJO events (which vary significantly from event to event) can be such as to reduce the drought (when the convective phase of a strong MJO passes over) or even to enhance the drought (dry phase of the MJO coincides with the drought).

6. Conclusions

The intraseasonal variability in the eastern Pacific warm pool in summer is well represented by a regional coupled model that is forced at the boundaries by observed meteorological fields during 1998-2003. Correlations between the model and observations in the east Pacific warm pool are 0.8 for 850hPa zonal wind anomalies and 0.6 for OLR anomalies. The phasing, amplitude, and propagation of OLR variability and associated lower tropospheric winds agree well between model and observations.

In the coupled model, evaporation is in phase with convection in the eastern warm pool, and appears to be most sensitive to low level wind speed (rather than SST), in agreement with limited observations in the region (such as the Tropical Atmosphere Ocean array, see Maloney and Esbensen 2007). This may be compared with observations in the eastern hemisphere that show evaporation in phase with convection or lagging convection by about one week (summarized in Hendon 2005). These phase relationships are at odds with the classic WISHE mechanism which applies for background mean easterlies (Emanuel 1987; Neelin et al. 1987), but other models have suggested that an unstable propagating mode can exist when the convection and evaporation are in phase, or evaporation slightly lags precipitation, in regions of background westerly flow or no basic flow (Xie et al. 1993; Raymond 2001; Sobel and Gildor 2003; Sobel et al. 2008).

The strength of the intraseasonal variability in the coupled model, as measured by the variance of outgoing longwave radiation, is close in magnitude to that observed, but with a maximum located about 10º to the west of the observed maximum off the Pacific coast of soutrhern Mexico. When the ocean model component is replaced by weekly reanalysis SST in an atmosphere-only experiment, there is a slight improvement in the location of the highest variance (due to differences in the climatological mean SST fields in the experiments), but there is a slight worsening of the lag correlations between model and observed OLR variability. Analysis of sensitivity experiments with the atmosphere-only model reveal a weak sensitivity of the intraseasonal OLR variability to 20-90 day SST variability. SST variability does not have a large effect either on the latent heat flux or on the low level convergence anomaly fields on intraseasonal timescales. It appears that the SST in the coupled model responds passively to anomalies of latent heat flux and short wave radiation that accompany intraseasonal convection events.

The intraseasonal wind anomaly patterns in the coupled model are consistent with the response to local heating in a linear baroclinic model. Observations and the regional coupled model indicate a dipole in intraseasonal convection anomalies in the east Pacific centered about 120° W. The linear barotropic model results suggest that the wind speed response to heating will change sign across 120° W, implying that the latent heat flux anomalies will do the same if they are primarily forced by wind speed, which appears to be the case. Indeed, analysis of the regional model results show that there is a dipole of wind speed anomalies; however, latent heat flux anomalies do not exhibit a dipole pattern in the regression fields, possibly due to weaknesses in the linear regression approach. The circulation response predicted by the linear model would lead to positive feedbacks to enhance convection (e.g. by increasing low level convergence and evaporation). This suggests that local convection-circulation feedbacks are important to intraseasonal convection in this region.

East Pacific intraseasonal convection appears to be influenced by the passage of the MJO signals from the boundaries, together with feedbacks between the circulation and convection. One possibility for the initiation of convection in the Eastern Pacific warm pool relates to the coincident suppression of convection in the eastern Hemisphere and propagation of a corresponding ‘dry’ intraseasonal Kelvin wave from the west Pacific. On reaching the eastern Pacific warm pool, frictional convergence at its northern flank, combined with the extensive area of warm SST, as well as possible wind-evaporation feedbacks, favors (and set the phase of) deep convection anomalies.

Acknowledgements

The constructive comments of two anonymous reviewers helped improve this paper. The majority of this work was done whilst R. J. S. and S. P. dS were at the International Pacific Research Center. S.-P. X, and R. J. S. were supported by NASA (grant NAG-10045 and JPL contract 1216010). S.-P. X, S. P. dS and R. J. S.were also supported by the Japan Agency for Marine-Earth Science and Technology (JAMSTEC) through its sponsorship of the International Pacific Research Center, and Japan Ministry of Education, Culture, Science and Technology through the Kyosei-7 Project. S.-P. X received additional support from the National Oceanic and Atmospheric Administration (NOAA) under grant NA07OAR4310257. IPRC contribution number XXX and SOEST contribution number YYY. EDM was supported under Award# NA05OAR4310006 from NOAA, and by the Climate and Large-Scale Dynamics Program of the National Science Foundation under Grants ATM-0832868 and ATM-0828531. The statements, findings, conclusions, and recommendations do not necessarily reflect the views of NSF, NOAA, or the Department of Commerce.

References

Back, L. E., C. S. Bretherton (2006) Geographic variability in the export of moist static energy and vertical motion profiles in the tropical Pacific. Geophys Res Lett 33: doi:10.1029/2006GL026672.

Barlow M, Salstein D (2006) Summertime influence of the Madden-Julian Oscillation on daily rainfall over Mexico and Central America. Geophys Res Lett 33: doi:10.1029/2006GL027738.

Barnett TP (1983) Interaction of the monsoon and Pacific trade wind system at interannual time scales Part I: The equatorial zone. Mon Wea Rev 111: 756–773.

Bessafi M, Wheeler MC (2006) Modulation of south Indian Ocean tropical cyclones by the Madden-Julian Oscillation and convectively-coupled equatorial waves. Mon Wea Rev 134: 638-656.

Bond NA, Vecchi GA (2003) On the Madden Julian Oscillation and precipitation in Oregon and Washington. Weath Forecast 18: 600-613.

Chang C-H (2009) Subseasonal variability induced by orographic wind jets in the East Pacific warm pool and South China Sea. Ph.D. dissertation, Univ. Hawaii, pp154.

Chiang JCH, Zebiak SE, Cane MA (2001) Relative roles of elevated heating and surface temperature gradients in driving anomalous surface winds over tropical oceans. J Atmos Sci 58: 1371-1394.

Chelton DB, Freilich MH, Esbensen SK (2000) Satellite Observations of the Wind Jets off the Pacific Coast of Central America. Part I: Case Studies and Statistical Characteristics. Mon Wea Rev 128**:**1993–2018.

Emanuel KA (1987) An air-sea interaction model of intraseasonal oscillations in the Tropics. J Atmos Sci 44: 2324-2340.

Farrar JT, Weller RA (2006) Intraseasonal variability near 10ºN in the eastern tropical Pacific Ocean. J Geophys Res 111, doi:10.1029/2005JC002989.

Fiedler PC, Talley LD (2006) Hydrography of the eastern tropical Pacific: a review. Prog Oceanogr 69: 143-180.

Flatau M, Flatau PJ, Phoebus P, Niiler PP (1997). The feedback between equatorial convection and local radiative and evaporative processes: The implications for intraseasonal oscillations. J Atmos Sci 54: 2373-2386.

Gill AE (1980). Some simple solutions for heat-induced tropical circulation. Quart J Roy Met Soc 106: 447-462.

Gilman D, Fuglister P, Mitchell JM (1963) On the power spectrum of red noise. J Atmos Sci 20: 182-184.

Garabowski WW (2006) Impact of explicit atmosphere-ocean coupling on MJO-like coherent structures in idealized Aquaplanet simulations. J Atmos Sci, 63, 2289-2306.

Hendon HH (2005) Air-Sea Interaction. In Lau WKM, Waliser DE (ed) Intraseasonal variability in the Atmosphere-Ocean Climate System, Springer, New York, pp 223-246.

Hendon HH, Glick J (1997) Intraseasonal air-sea interaction in the tropical Indian and Pacific Oceans. J Clim 10:647-661.

Hendon HH (2000) Impact of air-sea coupling on the Madden-Julian oscillation in a general circulation model. J Atmos Sci 57:3939-3952.

Higgins RW, Chen Y, Douglas AV (1999) Interannual variability of the North American warm season precipitation regime. J Clim 12:653-680.

Horel JD (1984) Complex principal component analysis: Theory and examples. J Applied Meteor *23*:1660–1673.

Hu Q, Randall DA (1994) Low-frequency oscillations in radiative-convective systems. J Atmos Sci 51:1089-1099.

Inness PM, Slingo JM (2003a) Simulation of the Madden-Julian Oscillation in a coupled general circulation model. Part 1: Comparison with observations and an atmosphere-only GCM. J Clim 16:345-364.

Innes PM, Slingo JM, Guilyardi E, Cole J (2003b) Simulation of the Madden-Julian Oscillation in a coupled general circulation model. Part II. The Role of the Basic State. J Clim 16:365-382.

Jiang X, Waliser DE (2008) Northward Propagation of the Subseasonal Variability over the Eastern Pacific Warm Pool, Geophys Res Lett doi:10.1029/2008GL033723.

Kalnay E, Coauthors (1996) The NCEP/NCAR 40 year re-analysis project. Bull Amer Meteor Soc 77: 437-471.

Kayano MT, Kousky VE (1999) Intraseasonal (30-60 day) variability in the global tropics: Principal modes and their evolution. Tellus 51A:373-386.

Kessler WS, McPhaden MJ, Weickmann KM (1995) Forcing of intraseasonal Kelvin waves in the equatorial Pacific. J Geophys Res 100:10613-10631.

Kessler WS (2002) Mean three-dimensional circulation in the northeast tropical pacific. J Phys.Oceanogr 32:2457-2471.

Legeckis R (1977) Long waves in the eastern equatorial Pacific Ocean: a view from a geostationary satellite. Science 197:1179-1181.

Liang J-H, McWilliams JC, Gruber N (2009) High-frequency response of the ocean to mountain gap winds in the northeastern tropical Pacific. J Geophys Res 114, doi:10.1029/2009JC005370.

Liebmann B, Smith CA (1996) Description of a complete (interpolated) Outgoing Longwave Radiation Dataset. Bull Am Met Soc 77:1275-1277

Lin JL, Kiladis GN, Mapes BE, Weickmann KM, Sperber KR, Lin W, Wheeler MC, Scubert SD, Del Genio A, Donner LJ, Emori S, Gueremy JF, Hourdin F, Rasch PJ, Roeckner E, Scinocca JF (2006) Tropical intraseasonal variability in 14 IPCC AR4 climate models. Part I: convective signals. J Clim 19:2665-2690.

Lin J, Mapes B, Zhang M, Newman M (2004) Stratiform precipitation, vertical heating profiles, and the Madden-Julian Oscillation. J Atmos Sci 61:296-309

Madden RA, Julian PR (1994) Observations of the 40–50-Day Tropical Oscillation—A Review. Mon Wea Rev 122:814–837.

Magana V, Amador JA, Medina S (1999) The Midsummer drought over Mexico and Central America. J. Clim., 12:1577-1588.

Maloney ED, Hartmann DL (2000) Modulation of eastern north Pacific hurricanes by the Madden-Julian oscillation. J Clim 13:1451-1460.

Maloney ED, Hartmann DL (2001) The sensitivity of intraseasonal variability in the NCAR CCM3 to changes in convective parameterization. J Clim, 14:2015-2034.

Maloney ED, Kiehl JT (2002b) MJO-related SST variations over the tropical eastern Pacific during Northern Hemisphere summer. J Clim 15:675-689.

Maloney ED, Kiehl JT (2002a) Intraseasonal eastern Pacific precipitation and SST variations in a GCM coupled to a slab ocean model. J Clim 15:2989-3007.

Maloney ED, Esbensen SK (2003) The amplification of east Pacific Madden-Julian oscillation convection and wind anomalies during June-November. J Clim 16:3482-3497.

Maloney ED, Sobel AH (2004) Surface fluxes and ocean coupling in the tropical intraseasonal oscillation. J Clim, 17:4368-4386.

Maloney ED, Esbensen SK (2007) Satellite and buoy observations of intraseasonal variability in the tropical northeast Pacific. Mon Wea Rev, 135:3-19.

Maloney ED, Chelton DB, and Esbensen SK (2008) Subseasonal SST variability in the tropical eastern north Pacific during boreal summer. J Clim 21:4149-4167.

Maloney ED, Shaman J (2008) Intraseasonal variability of the west African monsoon and Atlantic ITCZ. J Clim 21:2898-2918.

Neelin JD, Held IM, Cook KH (1987) Evaporation-wind feedback and low frequency variability in the tropical atmosphere. J Atmos Sci 44:2341-2348.

North GR, Bell TL, Cahalan RF, Moeng FJ (1982) Sampling errors in the estimation of empirical orthogonal functions. Mon Wea Rev 110:699-706.

Pacanowski RC Griffies SM (2000) The MOM3 manual. GFDL Ocean Group Tech. Rep. 4, Geophysical Fluid Dynamics Laboratory, Princeton, N.J., 680pp. http://www.gfdl.noaa.gov/~smg/MOM/web/guide_parent/guide_parent.html.

Pacanowski RC, Philander SGH (1981) Parameterization of vertical mixing in numerical models of tropical oceans, J Phys Oceanogr. 11:1443-1451.

Raymond DJ, (2001) A new model of the Madden-Julian Oscillation. J Atmos Sci 58:2807-2819.

Reynolds RW, Rayner NA, Smith TM, Stokes DC, Wang W (2002) An improved in situ and satellite SST analysis for climate. J Clim 15:1609-1625.

Reynolds RW, Smith TM, Liu C, Chelton DB, Casey KS,Schlax MG (2007) Daily High-Resolution-Blended Analyses for Sea Surface Temperature. J Clim 20: 5473-5496.

Seo H, Miller AJ, Roads JO (2007) The Scripps Coupled Ocean-Atmosphere Regional (SCOAR) Model, with applications in the Eastern Pacific sector. J Clim, 20:381-402.

Slingo JM, and co-authors (1996) Intraseasonal oscillations in 15 atmospheric general circulation models: results from an AMIP diagnostic subproject. Clim Dyn 12:325-357.

Small RJ, deSzoeke SP, Xie S-P (2007) The Central American Mid-summer Drought: regional aspects and large scale forcing. J Clim 20: 4853–4873.

Sobel AH, Gildor H (2004) A simple time-dependent model of SST hot spots. J Clim 16:3978-3992.

Sobel AH, Maloney ED, Bellon G, Frierson DM (2008) The role of surface heat fluxes in tropical intraseasonal oscillations. Nature Geoscience, 1:653 – 657.

Sobel AH, Maloney ED, Bellon G, Frierson DM (2010) Surface fluxes and tropical intraseasonal variability: a reassessment. J Adv Model Earth Syst, in press.

Thompson RM, Payne SW, Recker EE, Reed RJ (1979) Structure and properties of synoptic scale wave disturbances in the Intertropical Convergence Zone of the Eastern Atlantic. J Atmos Sci, 36,: 53-72.

Waliser DE, Lau KM, Kim JH (1999) The influence of coupled sea surface temperatures on the madden-Julian Oscillation: a model perturbation experiment. J Atmos Sci 56:333-358.

Wang B (2005) Theory. In Lau WKM, Waliser DE (ed) Intraseasonal variability in the Atmosphere-Ocean Climate Syetem, Springer, New York, pp307-360.

Wang Y, Sen OL, Wang B (2003) A highly resolved regional climate model and its simulation of the 1998 severe precipitation events over China. Part I: Model description and verification of simulation. J Clim 16:1721-1738.

Wang B, Rui H (1990) Dynamics of the coupled mosit Kelvin-Rossby wave on an Equatorial β plane. J Atmos Sci 47: 397-413.

Wang B, Webster P, Kikuchi K, Yasunari T, Qi Y (2006) Boreal summer quasi-monthly oscillations in the global tropics. Clim Dyn 27:661-675.

Wang B, Xie X (1998) Coupled modes of the warm pool climate system. Part I the role of air-sea interaction in maintaining Madden Julian Oscillation. J Clim 11: 2116-2135.

Watanabe M, Kimoto M (2000) Atmosphere-ocean coupling in the North Atlantic: a positive feedback. Quart J Roy Met Soc 126:3343-3369.

Wentz FJ, Smith DK (1999) A model function for the ocean-normalised radar cross-section at 14 GHz derived from NSCAT observations. J Geophys Res, 104:11499-11514.

Wijesekera HW, Rudnick DL, Paulson CA, Pierce SD, Pegau WS, Mickett J, Gregg MC (2005) Upper ocean heat and freshwater budgets in the eastern Pacific warm pool. J Geophys Res 110, doi:10.1029/2004JC002511.

Woolnough SJ, Vitart F, Balmaseda MA (2007) The role of the ocean in the Madden-Julian Oscillation: implications for MJO prediction. Quart . Roy Met Soc 133:117-128.

Wu Z, Battisti DS, Sarachik ES (2000) Rayleigh friction, Newtonian cooling, and the linear response to steady tropical heating. J Atmos Sci 57: 1937-1957.

Wu Z, Sarachik ES, Battisti DS (2000) Vertical structure of convective heating and the three dimensional structure of the forced circulation in the tropics. J Atmos Sci 57: 2169-2187.

Wyrtki K (1964) Upwelling in the Costa Rica Dome. Fishery Bulletin 63:355-372.

Xie S-P, Hu K, Hafner J, Tokinaga H, Du Y, Huang G, Sampe T (2009) Indian Ocean capacitor effect on Indo-Western Pacific climate during the summer following El Nino. J Clim, 22:730-747.

Xie S-P, Kubokawa A, Hanawa K (1993) Evaporation-wind feedback and the organizing of tropical convection on the planetary scale. Part I: quasi-linear instability. J Atmos Sci 50:3873-3893.

Xie S-P, Miyama T, Wang Y, Xu H, deSzoeke SP, Small RJ, Richards KJ, Mochizuki T, Awaji T (2007) A regional ocean-atmosphere model for eastern Pacific climate: towards reducing tropical biases. J Clim, 20:1504-1522.

Xie S-P, Xu H, Kessler WS Nonaka M (2005) Air-sea interaction over the eastern Pacific warm pool: Gap winds, thermocline dome, and atmospheric convection. J Clim 18:5-25.

Zamudio, L, Hurlburt HE, Metzger WJ, Morey SL, O'Brien JJ, Tilburg C, Zavala-Hidalgo J (2006) Interannual variability of Tehuantepec eddies. J Geophys Res, **111** doi:10.1029/2005JC003182.

Zebiak SE (1986) Atmospheric convergence feedback in a simple model for El-Niño. Mon Wea Rev 114: 1263-1271.

Zhang C (2006) Madden-Julian Oscillation. Rev Geophys 43:2004RG000158.

Zhang C, Dong M, Gualdio S, Hendon HH, Maloney ED, Marshall A, Sperber KR, Wang W (2005) Simulations of the Madden-Julian oscillation in four pairs of coupled and uncoupled global models. Clim Dyn 21:573-592.

(a) Wind speed contribution

Relative humidity %	**SST-T_a (°C)**			
	0.5	**1**	**1.5**	**2**
80	5.2	5.5	5.9	6.2
75	6.4	6.7	7	7.4
70	7.5	7.8	8.2	8.5

(b) SST contribution

Relative humidity %	**SST-T_a (°C)**			
	0.5	**1**	**1.5**	**2**
80	0.21	0.21	0.21	0.21
75	0.26	0.26	0.26	0.26
70	0.32	0.32	0.32	0.32

Table 1. Relative contributions to evaporation (Wm^{-2}) of a) wind speed ΔE_W and b) SST (ΔE_{SST}) for a wind speed anomaly of $0.3ms^{-1}$, and an SST anomaly of 0.06°C,. Here the mean wind speed is $6ms^{-1}$, mean SST is 27°C, latent heat of vaporization ~ 2.5 10^{-6} , turbulent heat exchange coefficient C_E=1.5x10^{-3} , density of air ~ $1kgm^{-3}$, and the rate of change of saturation specific humidity with temperature ($\partial q_s/\partial T$=K) is given by 8.1x10^{-4} K^{-1}.

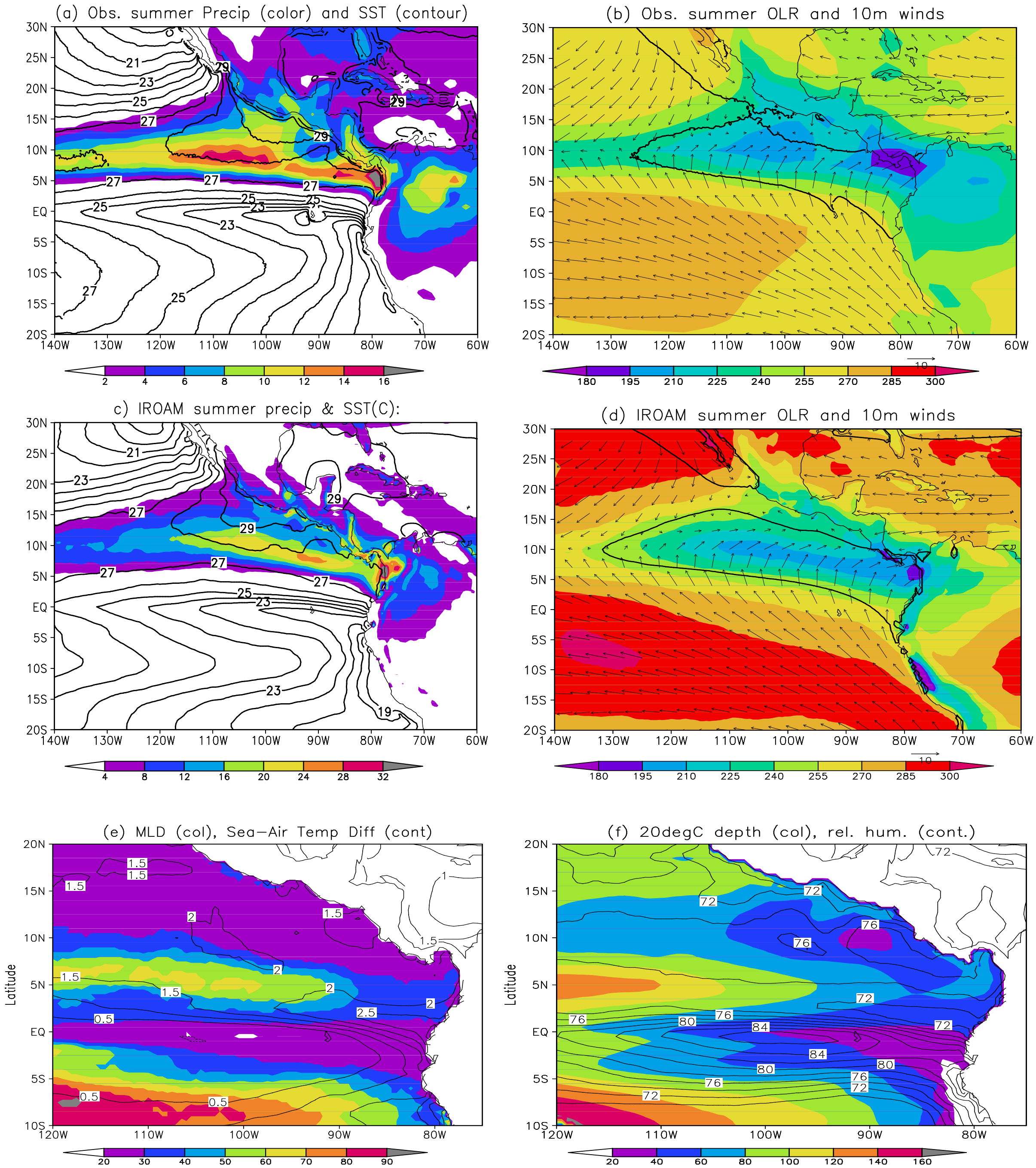

Figure 1. Summer climatology (June to September mean from 1998-2003) of the Eastern Tropical Pacific. a) Observed precipitation from TRMM 3B42 (color, mmday^{-1}) and SST from TMI (contours, ºC) b) Observed NOAA OLR (color, Wm^{-2}) and mean 10 m wind vectors from QuikSCAT (ms^{-1}). c) as a) but for the IROAM coupled model, SST and precipitation: note different color bar from a). d) as b) but for the coupled model OLR and mean wind vectors. In b) and d) the zero contour of 10m zonal wind is overlaid. e) Mixed layer depth (color, m) and sea minus air temperature difference (ºC, contour) from the coupled model f) depth of the 20ºC isotherm (color, m), and near-surface relative humidity (%) from the coupled model. Mixed layer depth is defined as the depth where the temperature is less than SST-0.2ºC.

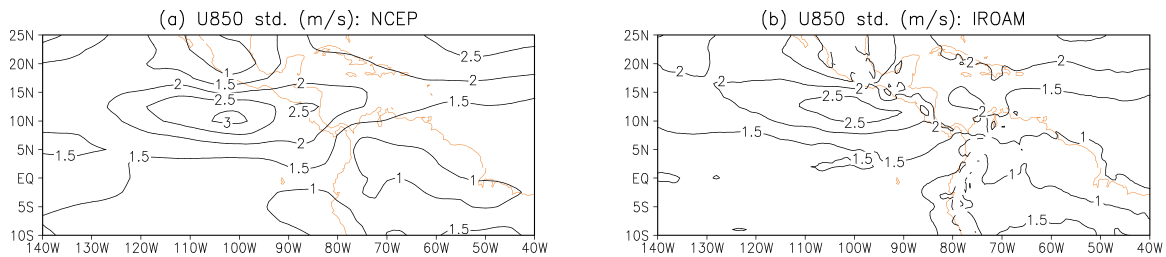

Fig. 2. Standard deviation of filtered zonal wind (ms^{-1}) at 850hPa, from 1998-2003, all seasons.

a) NCEP/NCAR reanalysis, and b) IROAM model.

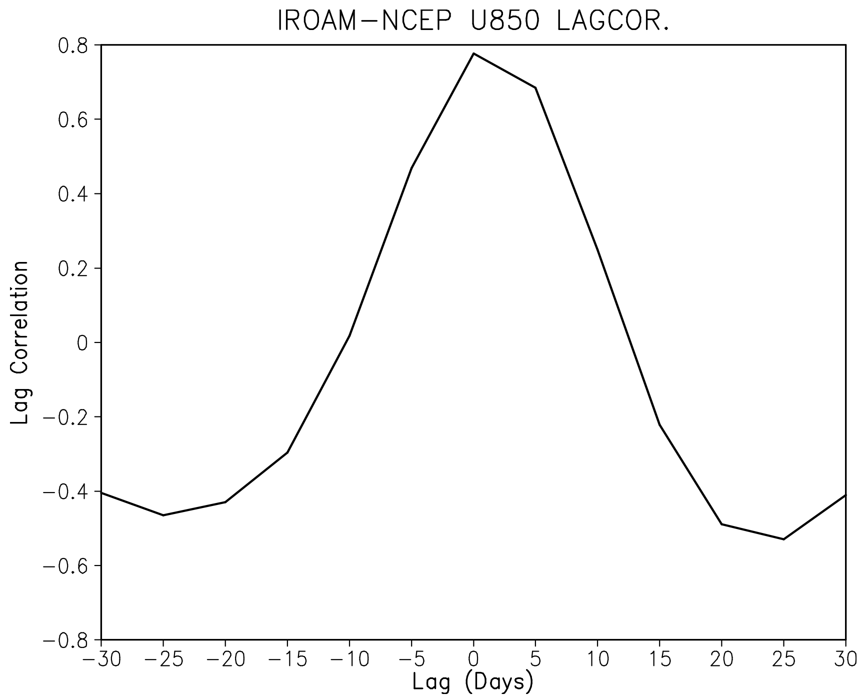

Fig. 3. Lag correlations, of IROAM filtered zonal wind at 850hPa onto NCEP filtered zonal wind at 850hPa, both averaged in the box 10°N to 15°N, 130°W to 100°W. Data is taken from 1998-2003, all seasons.

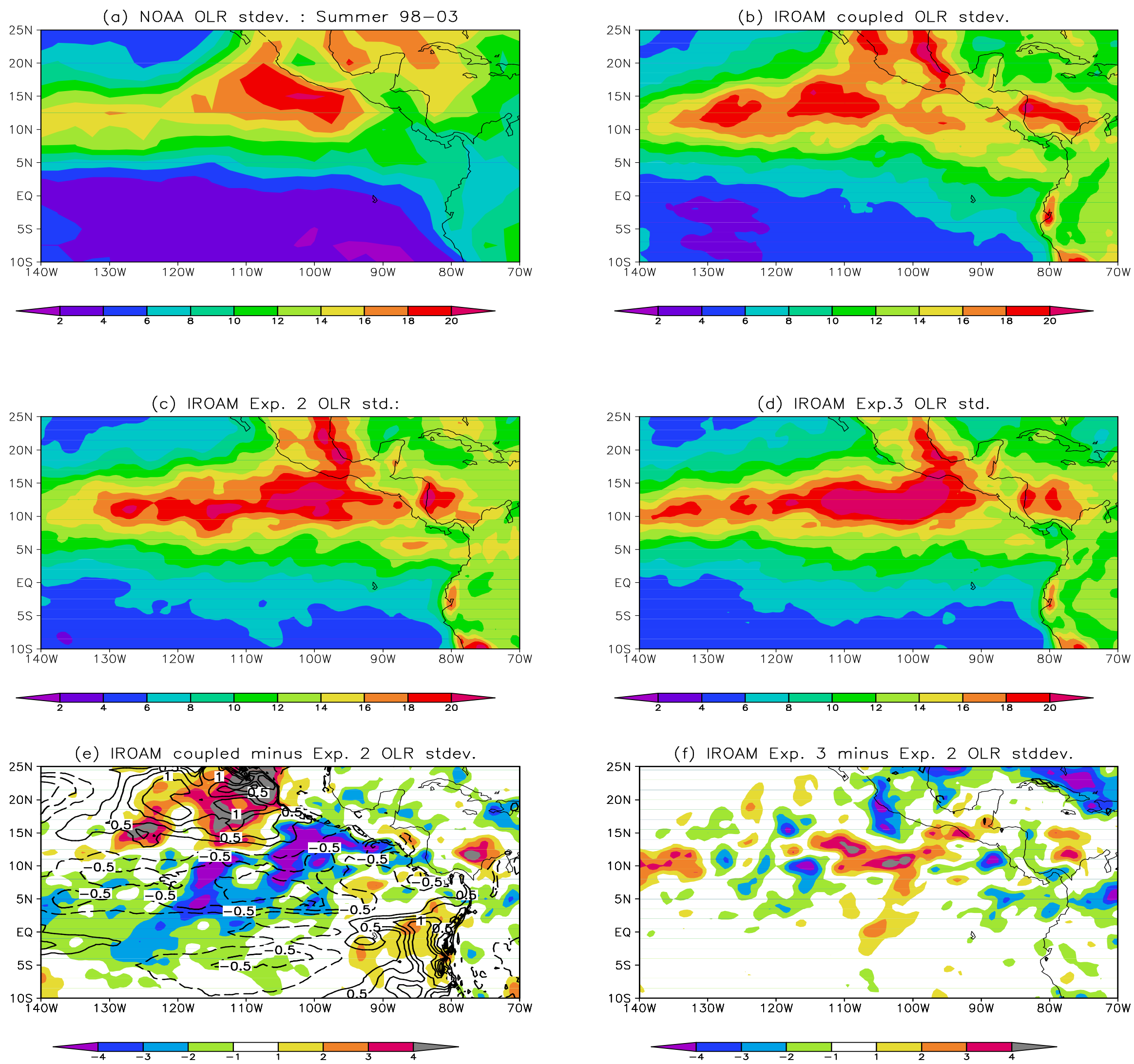

Figure 4. a),- d) Standard deviation of filtered OLR (color, Wm^{-2}): a) from NOAA observations, b) from the regional coupled model, Exp. 1, c) from the regional atmosphere-only model Exp. 2. and d) from the regional atmosphere-only model run with smooth SST, Exp. 3, e), f) differences in OLR standard deviation for e) Exp. 1 minus Exp. 2 and f) Exp. 3 minus Exp. 2. Data is taken from 1998-2003, summer season (Jun-Sep). The OLR from the IROAM model has been smoothed with a 1-3-1 filter in two dimensions. In e) the climatological summer mean SST difference of Exp. 1 minus Exp. 2 is contoured at 0.25ºC intervals, with negative values dashed, and the zero contour omitted.

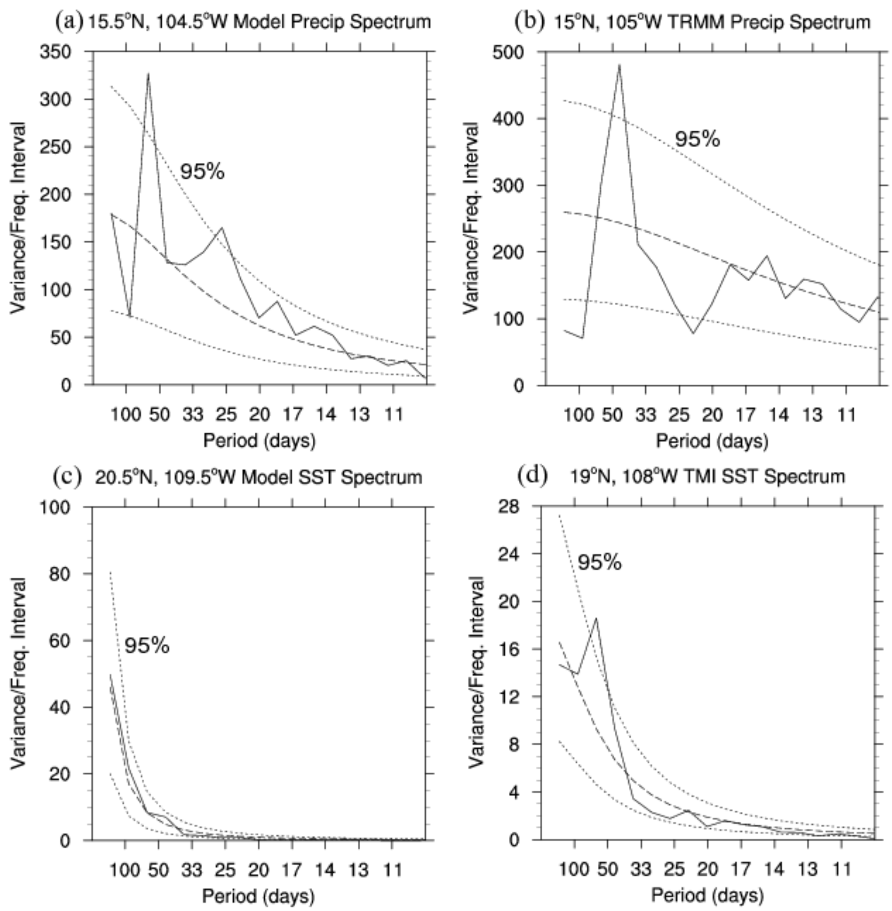

Figure 5. a, b) Power spectrum of May-October precipitation averaged over a 10^ox10^o box centered at a) 15.5°N, 104.5°W,coupled model and b)15°N, 105°W, from TRMM precipitation. c, d) SST averaged over a 4^ox4^o box centered c) at 20.5°N, 109.5°W for the coupled model and d) at 19°N, 108°W from TMI SST. The climatological seasonal cycle was removed before computation of the spectrum. Also shown are the red noise background spectrum and the 95% confidence limits on this background spectrum.

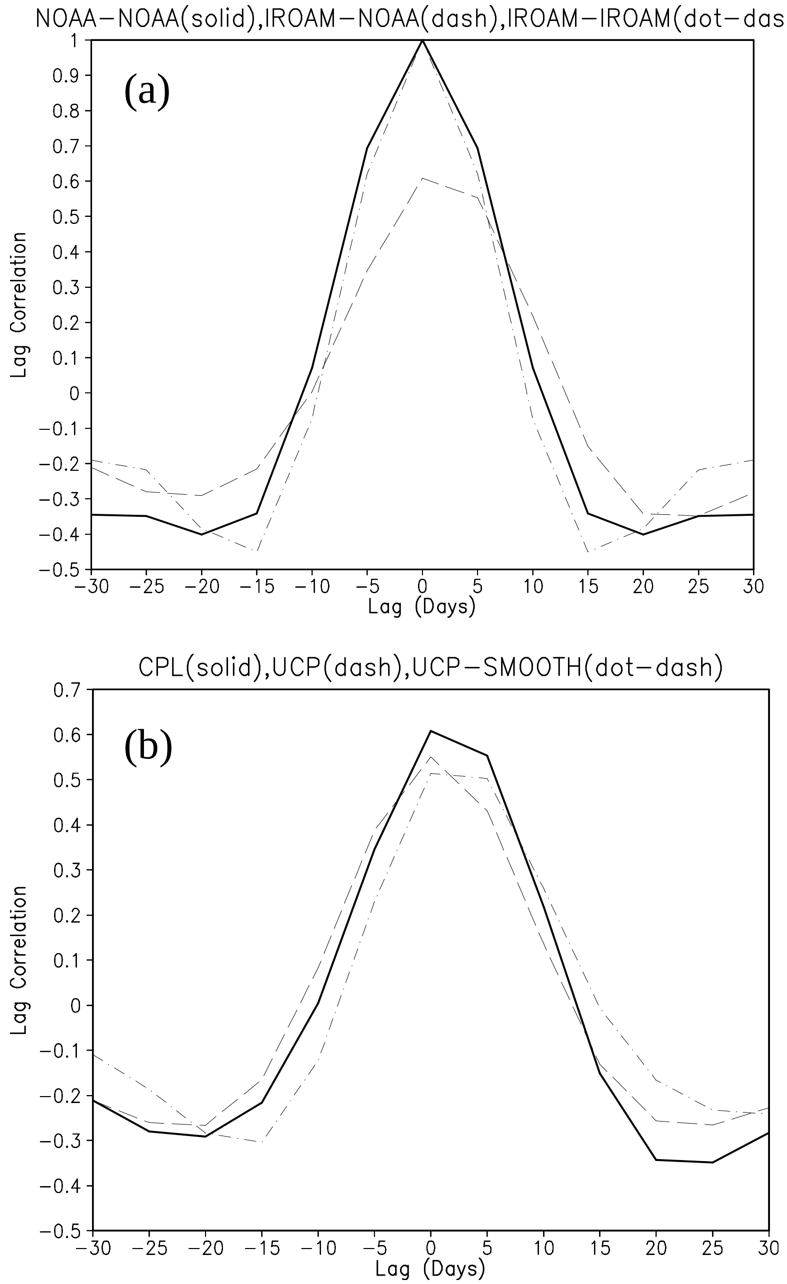

Fig. 6. Lag correlations of filtered OLR in the box 10°N to 20°N, 110°W to 100°W. a) NOAA OLR autocorrelation (solid line, symmetric), IROAM OLR autocorrelation (dash-dot line, symmetric) and the lag correlation of IROAM OLR onto NOAA OLR (dashed line). b) Lag correlations, of IROAM OLR onto NOAA OLR. Solid line: fully coupled run. Dashed line: atmosphere only run with Reynolds SST. Dot-dashed line: atmosphere only run forced with SST with no intraseasonal variability. Data is taken from 1998-2003, all seasons.

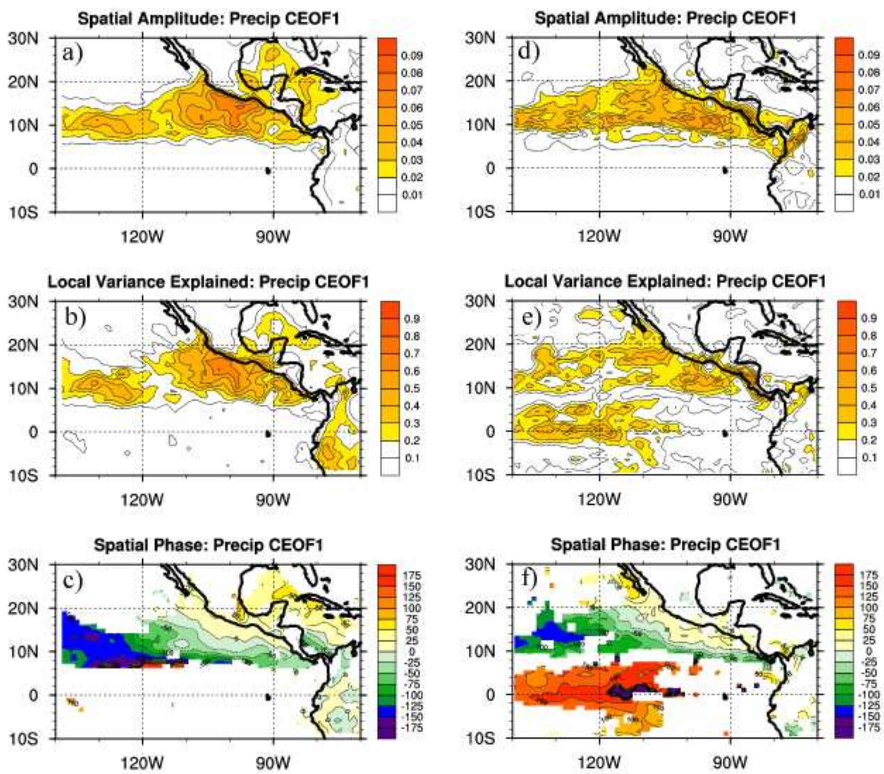

Figure 7. a) Spatial amplitude, b) fraction of local variance explained, and c) spatial phase corresponding to the first CEOF of June-October 30-90 day TRMM precipitation. d), e), f): as a), b), c) but for the coupled model, Exp. 1. The spatial amplitude was normalized in the calculation of the CEOFs. Increasing spatial phase indicated the direction of propagation for increasing temporal phase. (Spatial phase is shown where local variance explained exceeds 0.1.)

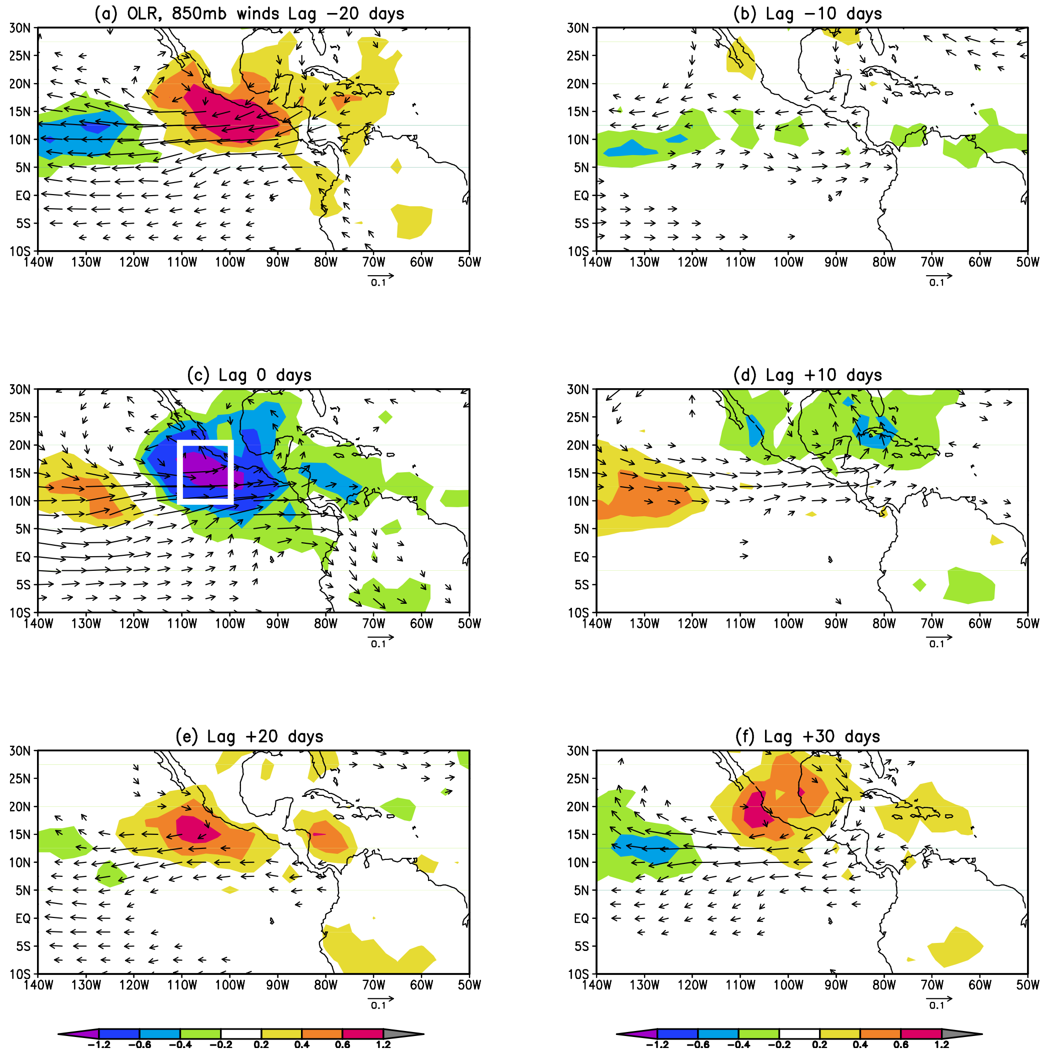

Figure 8. NOAA filtered OLR (color) lag regressed onto the filtered OLR in the 10°N to 20°N, 110°W to 100°W box area for various lags: a) -20 days, b) -10 days, c) 0 days, d) 10 days, e) 20 days and f) 30 days. Vectors show NCEP/NCAR reanalysis winds at 850hPa lag regressed onto the OLR index: every second point in longitude is shown, and only vectors with magnitude greater than 0.025ms^{-1}/Wm^{-2}. Panels show lags at intervals of 10 days. Negative OLR is associated with strong convection. White box in c) denotes the area used for linear regression.

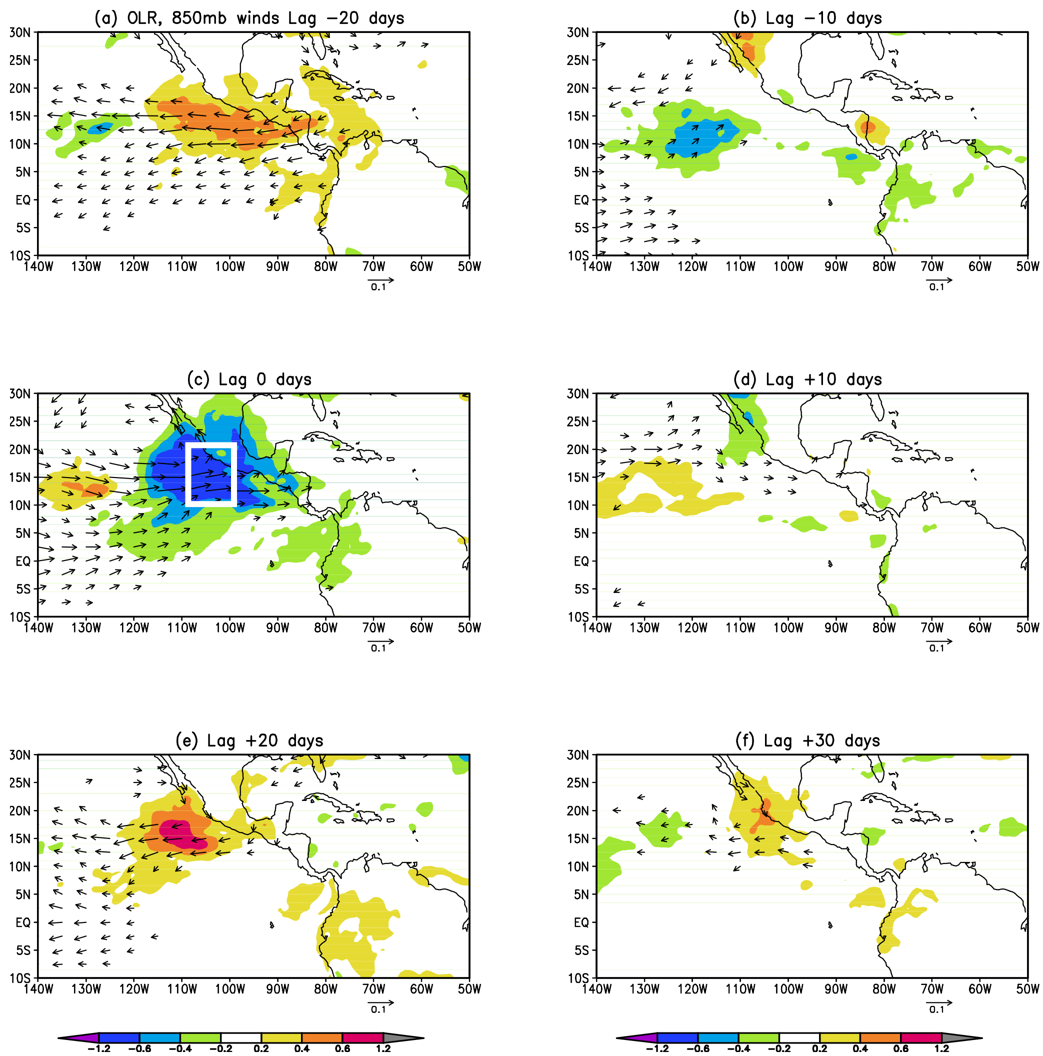

Figure 9. As Figure 8 but from regional coupled model (IROAM): filtered OLR lag regressed onto the IROAM filtered OLR in the 10°N to 20°N, 110°W to 100°W box.

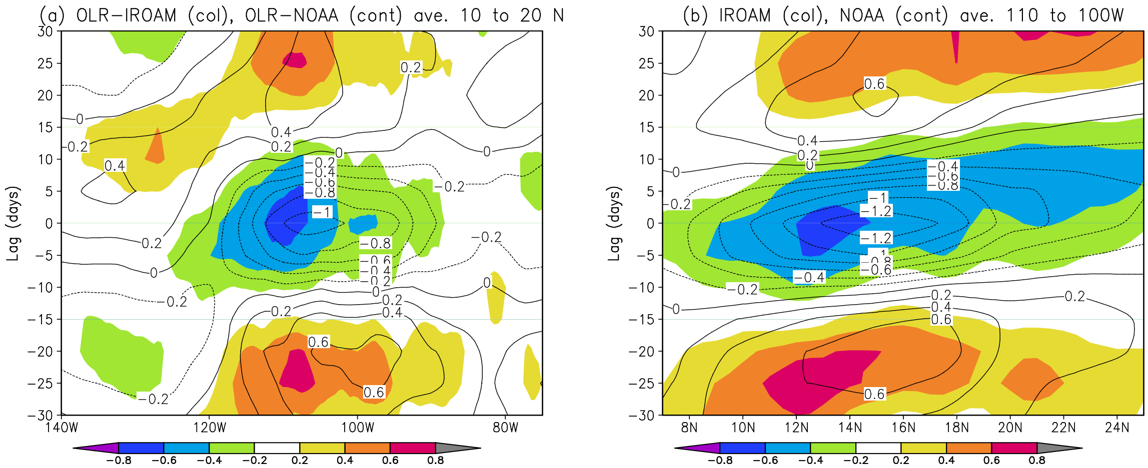

Figure 10. a), b) IROAM OLR lag regressed onto NOAA OLR index (col): NOAA OLR lagged onto NOAA OLR index (contour). a) shows a Hovmoller diagram for an average between 10° and 20°N, indicating eastward propagation and b) shows a Hovmoller diagram for data averaged between 110° to 100° W, to illustrate northward propagation.1998-2003 data, summer.

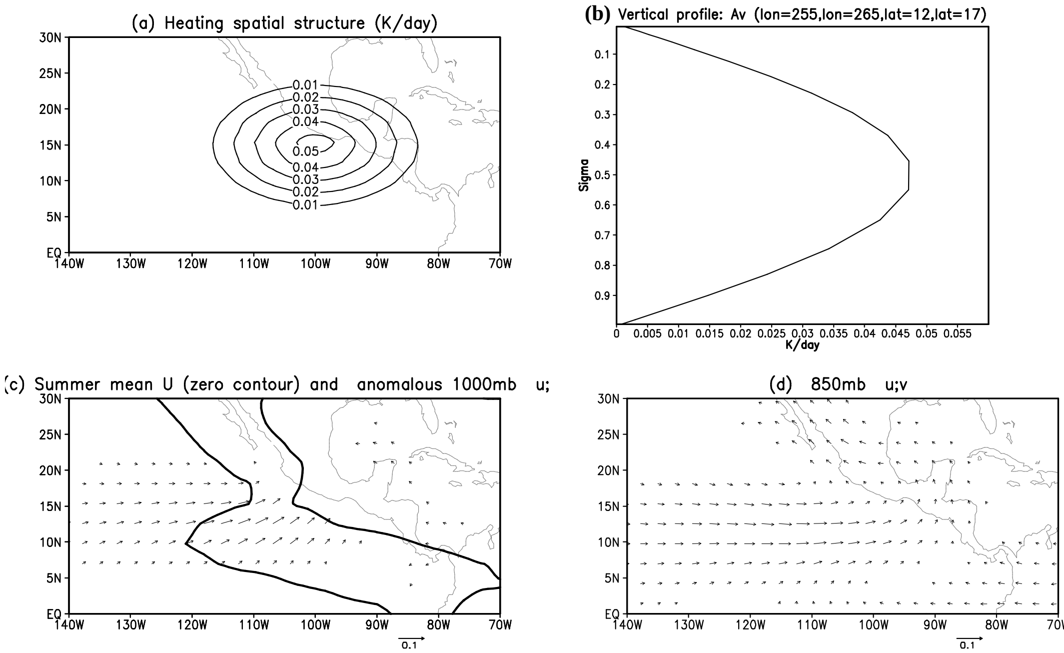

Figure 11. Linear baroclinic model simulations of the response to a heat source over the Eastern Pacific in summer. a) horizontal structure (heating rate in Kday^{-1} at σ=0.55), b) vertical structure plotted against σ(Kday^{-1}, area-average as labeled), c) model-simulated 1000hPa wind response (ms^{-1}) and the zero contour of the background summer-mean zonal wind from NCEP/NCAR reanalysis (mean westerlies are enclosed within the contour), and d) model-simulated 850hPa wind response (ms^{-1}).

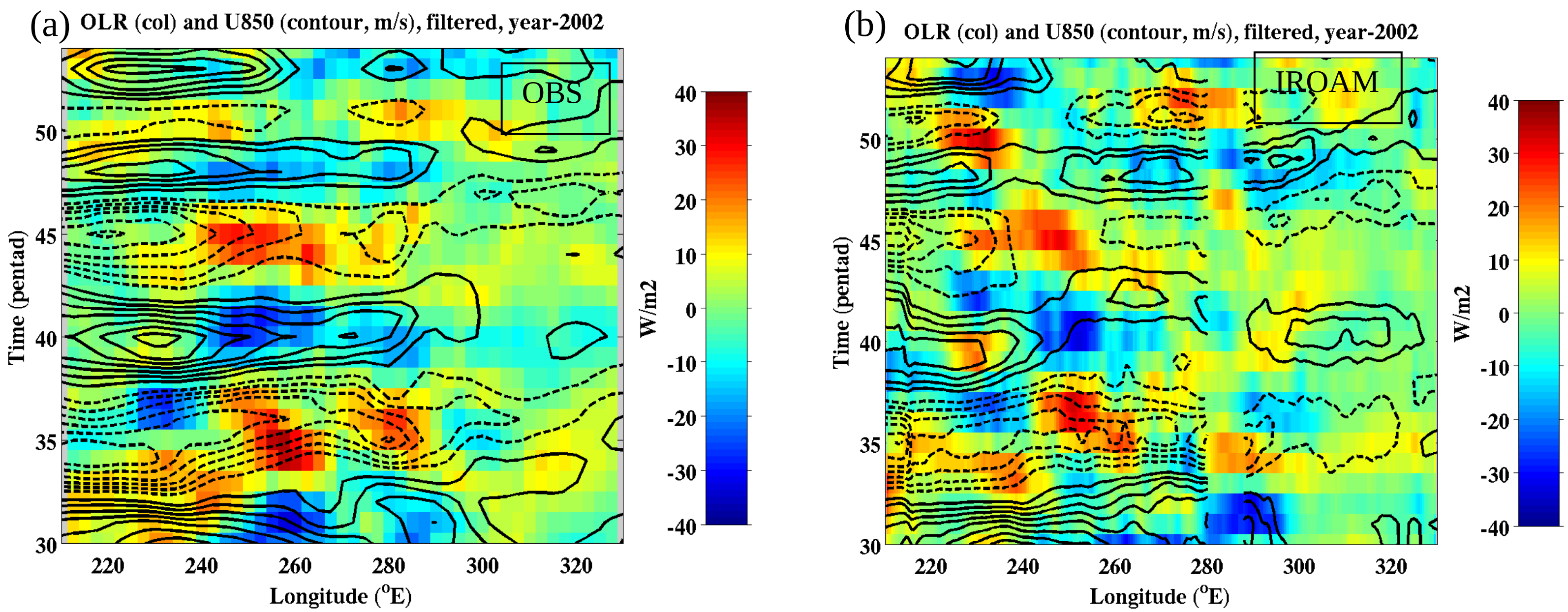

Figure 12. Hovmoller plots of OLR (color, Wm^{-2}) and 850hPa zonal wind (U850, contoured at 0.5ms^{-1} intervals, negative dashed and zero omitted), both filtered. OLR is averaged between 10ºN and 20ºN, whilst U850 is averaged between 10ºS and 10ºN. Note these plots cover the complete longitude domain of IROAM from 150W to 30W, allowing inspection of boundary conditions. a) OLR from NOAA and U850 from NCEP/NCAR reanalysis for 2002, as a function of pentad number (pentads 30 to 53 span the June to September period). b) corresponding fields from IROAM.

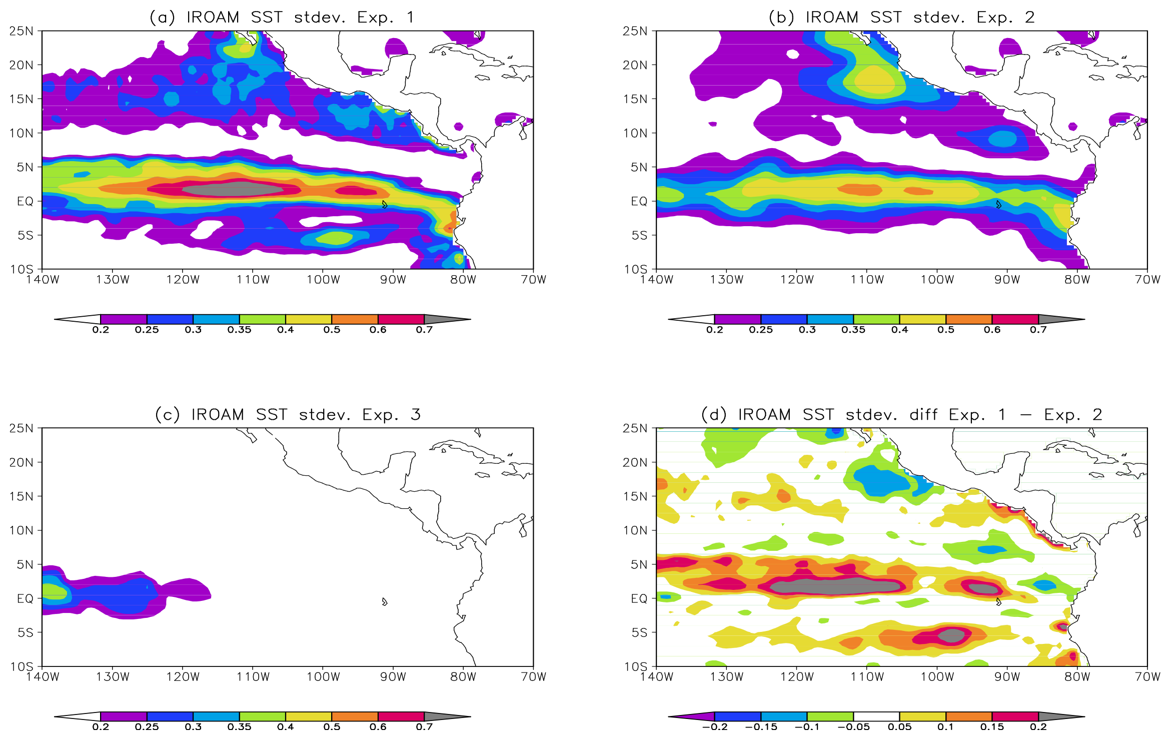

Figure 13. a), Standard deviation of 20-90 day filtered SST (ºC, see non-linear color scale) from the coupled model Exp. 1. b) as a) but for the Reynolds and Smith (2002) SST product, used as boundary conditions for the uncoupled run Exp. 2. c),as a) but from the atmosphere-only run with smoothed SST , Exp. 3, and d): difference of SST standard deviation between Exp. 1 and Exp. 2. Data from 1996-2003, summer season.

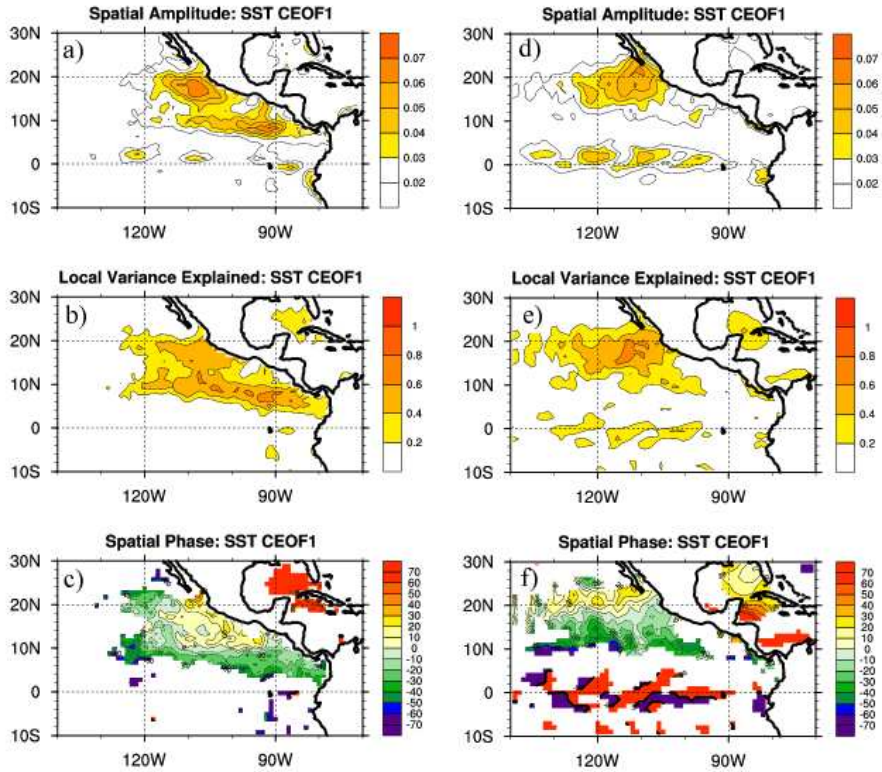

Fig. 14. a) Spatial amplitude, b) fraction of local variance explained, and c) spatial phase corresponding to the first CEOF of June-October 30-90 day observed (TMI) SST. d), e), and f), as above but for the coupled model, Exp. 1. The spatial amplitude was normalized in the calculation of the CEOFs. Increasing spatial phase indicated the direction of propagation for increasing temporal phase.

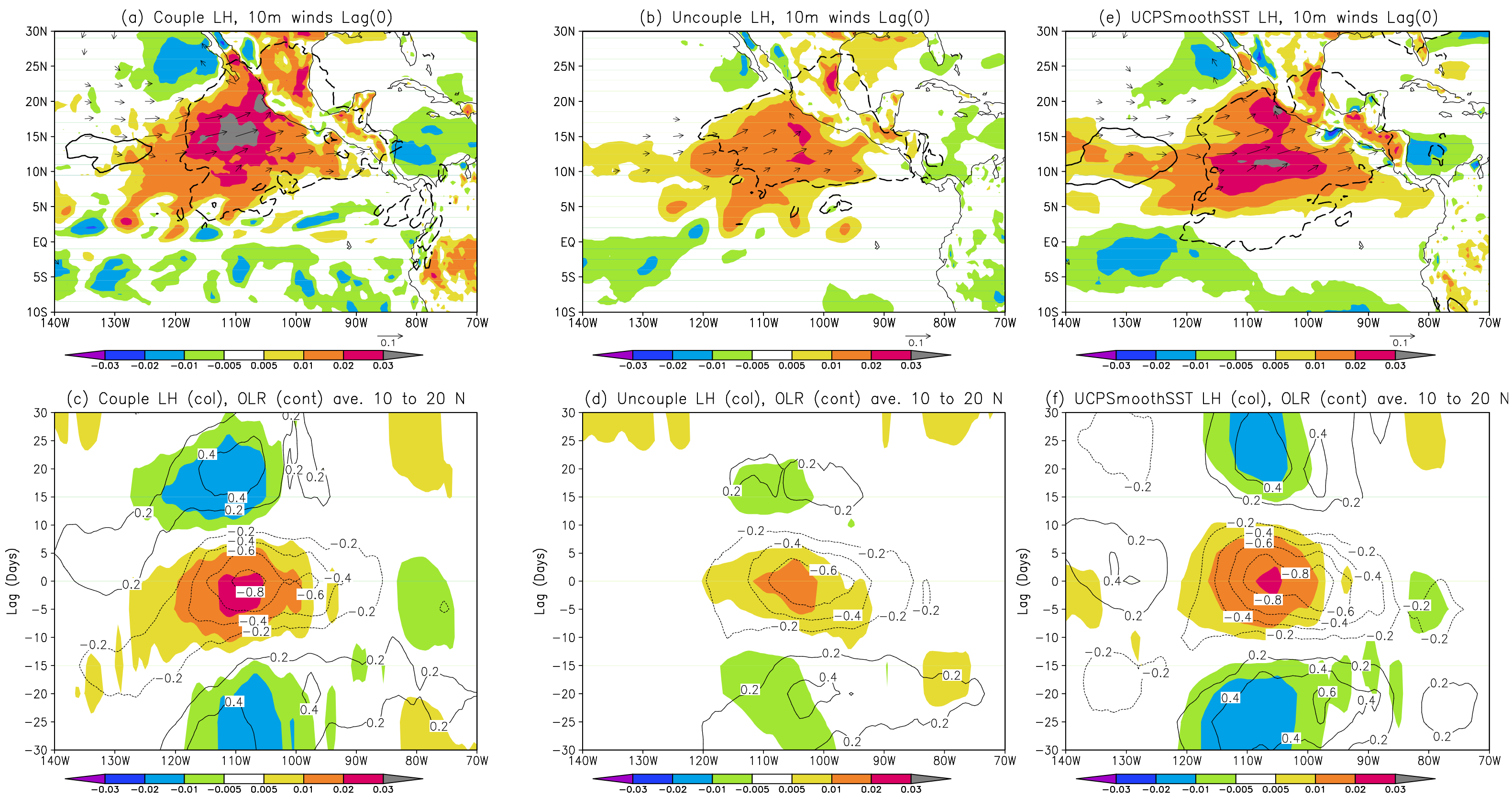

Figure 15. a). IROAM filtered evaporation lag regressed onto the IROAM OLR index: lag (0days) (mmday^{-1} per Wm^{-2}, color) for Exp. 1. The +/-0.3 OLR regression contour is overlaid for reference, and 10m wind regressions are shown as vectors (scale arrow at bottom right of each plot, units ms^{-1} per Wm^{-2}). c) Hovmoller plot of the evaporation regression (color) averaged between 10ºN and 20ºN, with OLR contours overlaid, for Exp. 1. b), d) as above but for uncoupled run Exp. 2. e, f) as above but for uncoupled, smooth SST run Exp. 3. 1998-2003 data, summer.

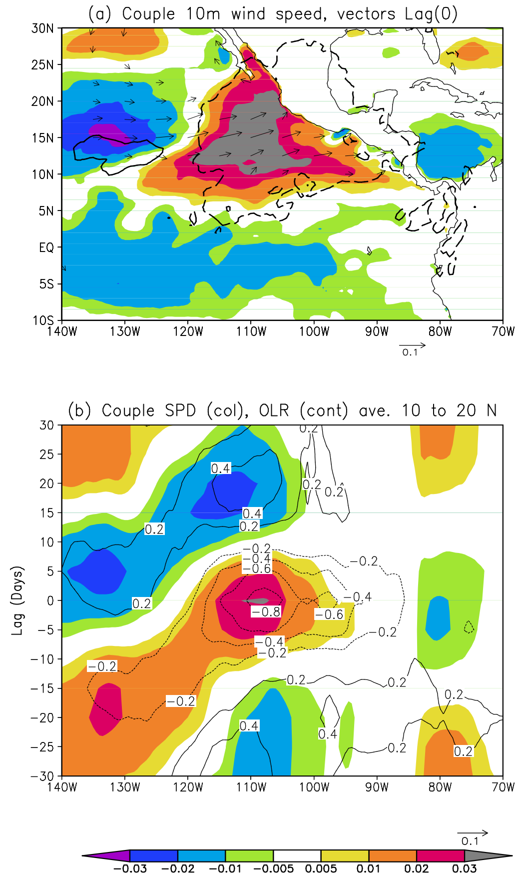

Figure 16. Maps of the IROAM filtered 10 m scalar wind speed (color) and 10 m wind vectors (arrow) lag regressed onto the IROAM OLR index: a) at lag (0). The +/-0.3 OLR contour is overlaid for reference. b) Hovmoller plot of the wind speed regression (color) averaged between 10ºN and 20ºN, with OLR contours overlaid. Units for wind speed and vectors are ms^{-1} per Wm^{-2}. 1998-2003 data, summer.

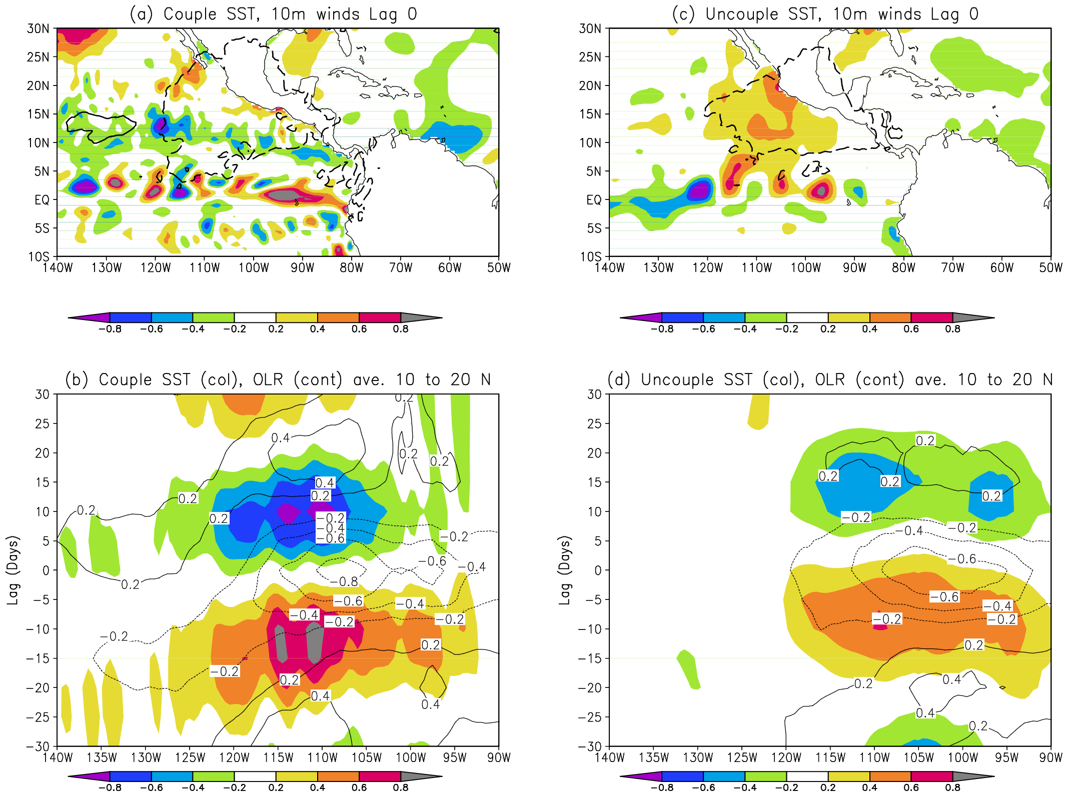

Figure 17. IROAM filtered SST (10^{-2} K per Wm^{-2}color) lag regressed onto the IROAM OLR index for Exp. 1. a) lag 0. The +/-0.3 OLR contour is overlaid for reference. b) Hovmoller plot of the SST regression (color) averaged between 10ºN and 20ºN, with OLR contours overlaid. c), d) as above but for uncoupled run. 1998-2003 data, summer.

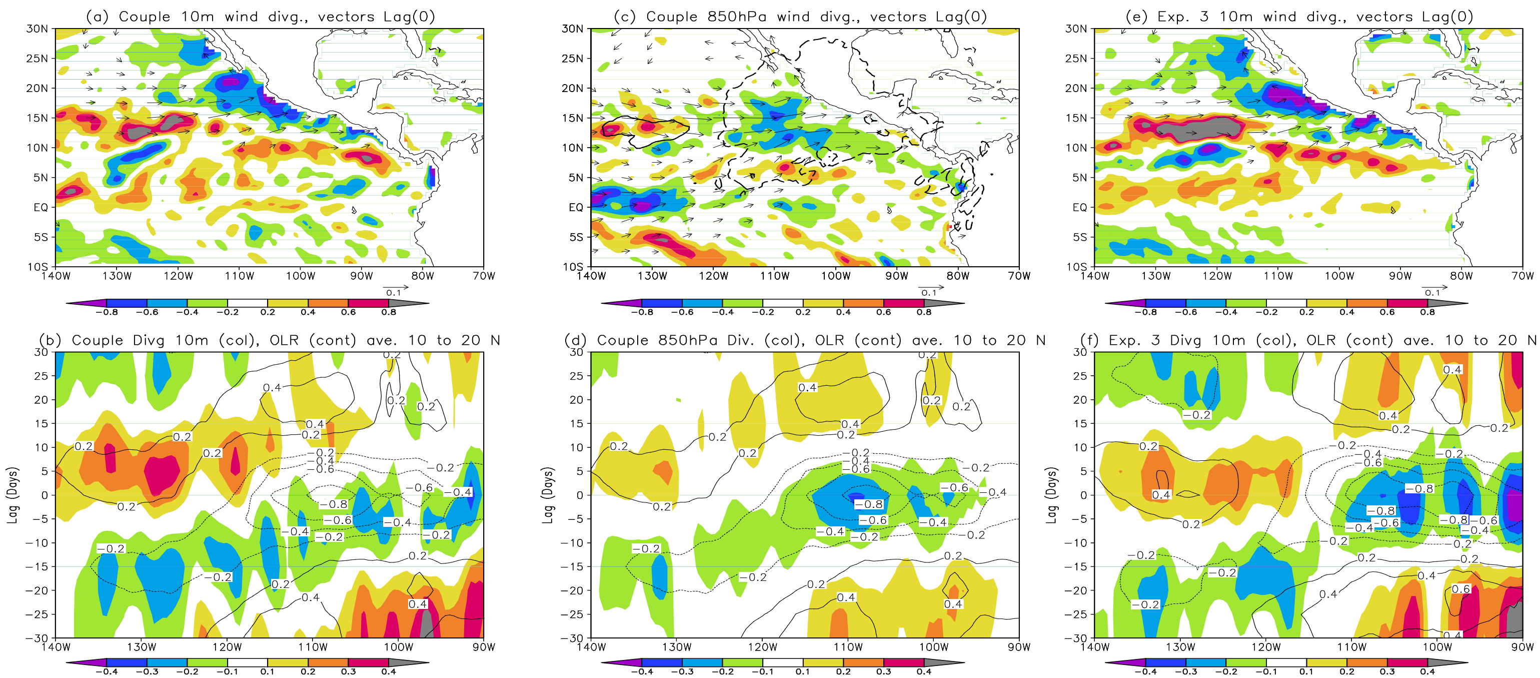

Figure 18. a) Map of the fully coupled IROAM filtered 10 m wind divergence (color) and 10 m wind vectors (arrow) lag regressed onto the IROAM OLR index at lag 0 (days). b) Hovmoller plot of the 10m wind divergence regression (color) averaged between 10ºN and 20ºN, with OLR contours overlaid. Units for divergence are $10^{-7}s^{-1}$ per Wm^{-2} and vectors are ms^{-1} per Wm^{-2}. Divergence has been smoothed twice with a 1-3-1 2-Dimensional filter. c), d) as a) b) above but for 850hPa winds from the coupled model. The +/-0.3 OLR contour is overlaid for reference. e, f) as a), b) above but for 10m winds from the atmosphere-only, smooth SST run Exp. 3. 1998-2003 data, summer.